Proceedings of International Conference on Violent Flows (VF-2007)
Organized by RIAM, Kyushu University, Fukuoka, Japan

Plunging Wave Breaking: EFD and CFD

Surajeet Ghosh, George Reins, Bonguk Koo, Zhaoyuan Wang, Jianming Yang, Fred Stern
IIHR - Hydroscience & Engineering, University of Iowa, Iowa City, IA, 52242, USA

Abstract

A complementary experimental and computational study of plunging breaking waves is presented that are generated in a two dimensional open channel flume using a bottom bump and impulsive accelerated flow. The time evolution of the transient wave and its flow properties are measured using experimental fluid dynamics (EFD): upstream and downstream velocity and flow rates using pitot probes; air-water interface elevation measurements and two dimensional particle image velocimetry in the wave breaking region. The computational fluid dynamics (CFD) methods are: Cartesian grid; embedded-boundary; hybrid HSM/GF/particle level set and VOF methods, and LES. CFD wave profiles at various time steps identifies the overall wave breaking process and major events: max wave height, first plunge, oblique splash-up, vertical jet, air entrainment, two repeats of these processes, dissipation and wave swept downstream which is qualitatively validated by EFD results. Both EFD and CFD results showed two subsequent plunging and splash-up events after the first plunge. After the wave breaks, the flow trends in mean velocity and vorticity observed in EFD are very similar to CFD which has more detailed resolutions of plunging, splashing, vertical jet and bubble entrainment. Current studies also revealed the occurrence of chaotic multiple splash-up events after the third plunging that produce span-wise vorticity and turbulence. Generation of a clockwise rotating bump vortex and an anticlockwise rotating span-wise wave breaking vortex that is created from the entrapped air after the breaking which transports turbulence from the trough towards the bulk fluid, were identified as the two important events. Mean values of turbulent kinetic energy (*TKE*) below the broken wave showed that the *TKE* levels increase by almost 90% after the first plunge and another 40% after the second plunge, after which as the wave is swept downstream by the accelerating mean flow the *TKE* dissipates.

Keywords: Plunging wave breaking process; Air-water interface; Mean velocity and turbulence; PIV; Cartesian/Embedded-boundary/VOF

1 Introduction

Wave breaking processes especially for plunging wave breaking are not yet well understood, including steep wave formation, jet overturning, splash-up, air entrainment, subsequent events, instabilities and organized vortices, and turbulence structures. Recent EFD and CFD have focused on qualitative descriptions of the wave breaking process; energy losses; 2D and 3D vortex and turbulent structures; wave impact; air entrainment; surf zone modeling; and multi-scale turbulence model. Tables 1 and 2 summarize the most relevant previous experimental and computational studies [1-7] on plunging breaking wave process and velocity and turbulence flow fields respectively.

The objectives of the present research are to provide a detailed quantitative description of the overall plunging wave breaking processes through complementary CFD and EFD at their current levels of resolution. Plunging wave breaking is generated by impulsive flow over a submerged bump fixed to the bottom of an open channel flume. The geometry is different from previous studies and of particular relevance to ship hydrodynamics, since the breaking involves body-wave interactions. The EFD includes the overall flow conditions (upstream, downstream, air-water interface elevation and flow rates) and phase averaged PIV velocities and turbulence inside the plunging breaking wave. The CFD simulations are carried out using a Cartesian grid solver with the LES for two-phase incompressible flows [8, 9]. The interface is represented by the level set method with the particle and VOF corrections for mass conservation, and the property jumps are treated with a combined Heaviside and Ghost Fluid Method. A sharp embedded boundary method is used to handle complex immersed boundaries on Cartesian grids.

2 Experimental Methods and Procedures

2.1 Facility, Model, Test Conditions and Procedures

The idea and approach of creating plunging breakers by using a bottom bump was obtained collectively from the works of previous researchers and the ongoing complementary CFD work at the Iowa Institute of Hydraulic Research. Miyata *et. al.* [10] examined two-dimensional shallow water flow over semicircular bumps to obtain a better understanding of the complicated flow behind a bluff body with separation and wave breaking. Iafrati *et. al.* [11] used

an unsteady Navier-Stokes solver for incompressible fluid coupled with a level set approach to describe complex free surface configurations and analyzed two-dimensional flow over a submerged bump. The bump (INSEAN) profile is given as follows,

$$z(x) = H(1 - 2x^2 / l^2 + x^4 / l^4) \quad (1)$$

where, l is half length of the bump, H is the bump height, x is the stream-wise direction and z is the vertical direction. The bump is suddenly started at $t = 0$, with $\zeta = z/H = 2.5$, $U = 1$ and $Fr_\zeta = 0.319$, where t is the time, U is the stream-wise velocity and Froude number (Fr) is based on the instantaneous water depth. Their analysis covered the successive stages of the wave breaking phenomenon viz. the steep wave formation, the falling jet, the splash-up and the air-entrainment and their numerical results qualitatively agreed with other experimental observations. Huang *et. al.* [12] applied coupled ghost fluid/two-phase level set method to simulate air/water turbulent flow involving complex geometries. They also applied their method for two dimensional flow over the INSEAN bump. Huang's test conditions were somewhat different from Iafrati *et. al.* [11]. They used sudden start at time $t = 0$ with $\zeta = 2.1$, $U = 1$ and $Fr_\zeta = 0.35$ and studied the wavy flow in a frame of reference moving with the bump. Huang *et. al.* [12] chose their test conditions based on the preliminary tests for the current experiments and their numerical results also agreed with available experimental data. The above studies showed that the flow over a submerged bump is a suitable experimental test case for creating plunging breakers provided the right flow conditions are achieved, which mainly depend on ζ, Fr_ζ and the aspect ratio AR.

The initial stages of the current research focused on finding the optimum flow conditions for generating the plunging breaker with wave heights more than 10cm and minimum surface tension effects according to Peregrine [1] in an open channel flume. The overall aim was to create repeatable plunging breaking waves which would ensure successful ensemble averaging of the experimental data thus making it useful for CFD validation. Breaking waves were created in an open channel flume (9 m long, 0.6m wide and 0.43 m high) using different bump sizes of semicircular profiles. Semicircular profiles were chosen since it was easily available at the experimental lab. However, the flume was too small and the pumps were not powerful enough to create high intensity plunging breakers of desired wave heights. To improve the results, further tests were carried out in a larger open channel flume (27m long, 0.91 m wide and 0.43m high). INSEAN bumps (equation 1) of different sizes were tested by suddenly starting the upstream flow similar to Iafrati *et. al.* [11]. It was observed that with increasing bump height the wave height also increased. After testing several flow conditions (vary flow acceleration and ζ) with different bump sizes the best results were obtained with a bump of height 11.43cm, $\zeta = 2$, $AR = 4.0$, and impulsive. With this arrangement it was possible to generate a single event unsteady plunging breaker of wave height approximately 10cm and negligible side wall disturbances. The flow was accelerated from stationary conditions such that the upstream Reynolds number (Re) and Fr based on the instantaneous water depth and mean velocity reached 50,000 and 0.36, respectively, at the time of breaking.

The side and plan views of the experimental setup are shown in Fig.1a and 1b. The figures show the flume to scale with the bump fixed at the flume bottom. Cartesian coordinate system is used where, x is the stream-wise direction, y is the span-wise direction and z is the vertical direction. The bump center is placed at $x = 0$ and $z = 0$ and the flume center plane is at $y = 0$. All length scales are normalized using the bump height H, unless otherwise mentioned. The flume is connected to two pumps each of 7.5Hp rating. The objective was to suddenly accelerate the fluid from zero to maximum velocity in the shortest time to replicate the impulsive start flow conditions as closely as possible and also create waves of maximum height. To achieve this both pumps are run simultaneously to attain maximum pump power. Each pump is controlled by a frequency driver where the pump speed is set using a frequency scale of range 0 - 60 Hz. After setting the initial stationary water depth $\zeta = 2$, the pumps are primed by vacuuming out any entrapped air in the areas of the pump lines that are above the flume water surface. The flow is accelerated from zero to a pump setting of 55 Hz within 7 seconds which corresponds to a mean upstream velocity, $\overline{U}_{ub}$, of 0.39 m/s at the time of breaking where, $\overline{U}_{ub}$ is averaged over the mean velocity profile outside the boundary layer. The flume has two pipes underneath the channel and each pipe is connected to each pump. The flow in the channel is from left to right while in the pipes it is from right to left as highlighted by the arrow in Fig.1a.

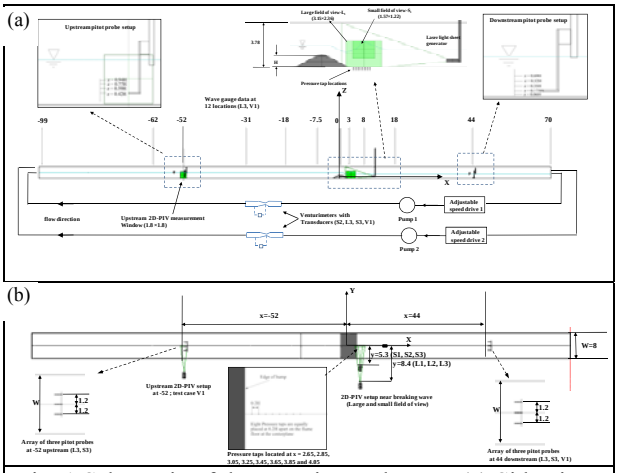

Fig. 1 Schematic of the experimental setup. (a) Side view. The upstream and downstream pitot probe arrangements are shown in close up views. The close up of the 2D PIV measurement areas near the wave breaking region is also shown. (b) Top view.

The experiments were conducted mainly to obtain 2D-PIV measurements inside the plunging breaker. However, it was necessary to fully document the flow conditions for successfully replicating the overall process using CFD and future experiments. Hence, measurements were also obtained to characterize the upstream and downstream flow conditions, overall air-water interface in the flume during the breaking and the flow rates. The inflow conditions were measured at an upstream location of x = -52

with both pitot probes and 2D-PIV and the downstream flow was measured at x = 44 using pitot probes only. The air-water interface elevation was measured using wave gauges at different stream-wise locations. The flow rates were measured from two venturimeters connected to the pipes below the flume. Six complete independent 2D-PIV measurements in the wave breaking region at the flume center plane were obtained. Three sets of measurements (L1, L2 and L3) were obtained with the PIV camera placed y = 8.4 away from the flume center plane to capture a large region around the breaking wave and three more with a smaller field of view (S1, S2, S3) to capture the details of the jet and entrapped air where the PIV camera was placed at y = 5.3 away from the center plane. Another set of 2D-PIV measurements (13 runs) was also obtained to measure the upstream velocity and turbulence (test case V1) where a video camcorder was placed to obtain images of the breaking wave with reference scales. The PIV results in the breaking wave region are presented only for L2 and S1 since for those cases the wave profiles at max height had the lowest standard deviation. The overall flow conditions data is presented for L3 and V1. Since the PIV data is unsteady it is first phase aligned and then ensemble averaged for calculating mean velocities and turbulence statistics. For each test case, measurements are repeated 22 times to achieve convergence of mean velocity and turbulence.

One of the concerns about the experiments was to achieve repeatability of the overall breaking process. The reconstruction of the coherent features and the turbulence statistics of the flow depend on the convergence of the means over several repeats of the experiment. The wave breaking event is considered repeatable if the wave just before breaking has the same maximum wave height at the same x location downstream of the bump which implies similar wave profiles before breaking.

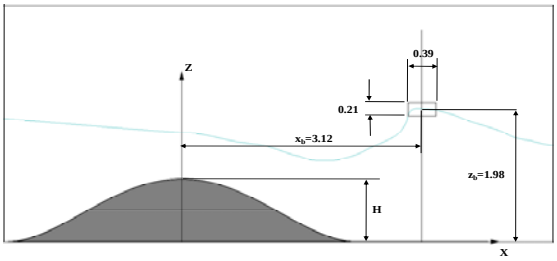

Fig. 2 Location of the highest point of the wave crest (x_b, z_b) at t_b with respect to the bump center. The wave profile shown here is from the mean of 22 runs from test case L3.

This is ensured by measuring the max wave height just before breaking. As an acceptable range, the x and the z coordinates of the crest should lie within ±6% of the mean horizontal x_b and mean vertical distance z_b from the bump center. The rectangular box as shown in Fig.2 highlights the acceptable region and illustrates the wave breaking criteria. The center of the box lies at x = 3.26 and z = 1.88. After starting the pumps the wave does not always break at the same exact time and so a reference parameter t_b is also defined as the time when the wave reaches its maximum height just before breaking. All wave breaking events have been phase aligned with respect to t_b. To generate a well controlled breaking wave it was necessary to allow a 30 minutes time gap between two successive runs that allows the initial water level to settle down and be absolutely calm. To confirm the accuracy of the initial water level, a wave gauge is used to check the air-water interface elevation and the acceptable error in the water level is ±0.02cm which is 0.1% of the initial water height. However, even after carefully setting the initial water height and priming of the pumps, the repeatability of the experiment is only 35%, which means that out of 100 runs 35 of them deliver successful plunging breaking event, which makes the overall process time consuming.

2.2 Measurement Systems, Data Acquisition Procedures and Data Reduction Equations

The flow measurements are sub-divided into six main data acquisition categories: inflow, out flow, air-water interface elevation, flow rate, and velocity, vorticity and turbulence flow fields under the breaking wave, and wave impact pressure. Time is defined as follows,

$$t' = t_b \pm \sum_{1}^{M} m\Delta t, \tag{2}$$

$$t = t' - t_b \tag{3}$$

where, the negative sign denotes pre-breaking and the positive sign denotes post-breaking, $\Delta t = 1/f$, where f is the data acquisition frequency and M is the total number of time steps pre or post breaking.

The upstream flow measurements are obtained using both LaVision PIV (test case V1) and United Sensors pitot probes. The probes are positioned with a spanwise spacing of Δy equal to 1.2 with the center probe located in the flume center plane. The probes are attached to a vertical traverse which allows for simultaneous movement in the z direction. A wave gauge placed at x = -62 and is used to trigger the data acquisition for the upstream PIV. After the pumps are started, as soon as the water level at x = -62 drops by $\Delta\zeta$ = -0.0175, the Labview program begins data acquisition for the wave gauges and transducers (venturi meters and downstream pitot probes) and sends a 5 Volt square sine wave to the PIV computer to begin acquiring data. Observations showed that the water level dropped by $\Delta\zeta$ = -0.0175 within 2 seconds after starting the pumps and the data acquisition time after that was sufficient to capture the overall breaking process. The PIV data is acquired at a data acquisition frequency of 7.5Hz for a total time of 20 seconds. The flow is seeded with neutrally buoyant silver coated glass spheres with an average diameter of 20 microns. The glass spheres are first mixed with water in a separate container and then the mixture is poured into the flume and the flume is run for approximately five minutes to achieve uniform seeding in the entire channel. The flume is seeded once every day before starting the experiments. A double pulsed underwater laser light sheet is fired from a light sheet generator placed at x = -48 towards the upstream direction in the flume center plane parallel to the stream-wise direction. Two Big Sky laser generators of 120mJ power and 532 nm wavelengths are used. The CCD camera of 1200×1600 pixel resolution and f/1.4-50mm focal length lens is placed outside the flume, looking per-

pendicularly to the laser light sheet plane. Before acquiring velocity data the camera is spatially calibrated so that the camera can identify the actual separation distance in mm and not in pixels in the object plane. Synchronization of laser and camera, data acquisition and image processing is done using LaVision hardware and DaVis 7.1 software. Data acquisition and parameter settings are facilitated using a Windows XP PC equipped with DaVis flow-master software. The decomposition of the instantaneous velocity into its mean and fluctuating components are given as follows,

$$u_i(t) = U(t) + u'(t) \tag{4}$$

$$w_i(t) = W(t) + w'(t) \tag{5}$$

where, u' and w' are the stream-wise and the vertical components of velocity fluctuations, respectively, and U and W are the ensemble averaged velocities [13],

$$U(t) = \lim_{N\to\infty} \frac{1}{N} \sum_{i=1}^{N} u_i(t) \tag{6}$$

$$W(t) = \lim_{N\to\infty} \frac{1}{N} \sum_{i=1}^{N} w_i(t) \tag{7}$$

where, u_i and w_i represent the instantaneous velocities of the i^{th} repeat of the experiment, and N is the total number of times the experiment is repeated. The upstream mean Re and Fr based on the instantaneous local water depth are,

$$\mathrm{Re}_{Zu}(t) = U_u(t)\mathrm{Z}_{-52}(t)H/\upsilon \tag{8}$$

$$Fr_{Zu}(t) = U_u(t)/\sqrt{g\mathrm{Z}_{-52}(t)H} \tag{9}$$

where, U_u is the mean upstream stream-wise velocity at x = -52, Z_{-52} is the mean air-water elevation at x = -52 (equation 14), υ is the kinematic viscosity and g is the gravitational acceleration.

For the downstream location velocity measurements are obtained using three pitot probes using a similar setup as the upstream location. All pitot probes are connected to Validyne pressure transducers, all with ranges of $\pm$ 2206.32 Pa, which are connected to a data acquisition board. All pressure transducers are statically calibrated with the high side of the transducer connected to a known water column and the low side left open to the atmospheric pressure. The water level on the high side is varied at 1cm increments and the corresponding output voltages are recorded in order to obtain a linear regression equation. The downstream pitot probe measurements are synchronized with the upstream PIV measurements and are both triggered by the wave gauge at x = -62. Unlike the upstream PIV data which is acquired at 7.5 Hz due to the limitations of PIV camera frequency, the pitot probe data is acquired at 100 Hz. However, the actual response frequency of all transducers were only 40Hz due to the plumbing response of the transducer and probe tubing combination. The total data acquisition time for PIV and pitot probes is kept the same at 20 seconds. The span-wise array of three pitot probes is moved at vertical increments of $\Delta\zeta$ = 0.175 starting from the flume floor to measure the exit velocity profile. The measurements are obtained at five different water depths viz. ζ = 0.06, 0.175, 0.35, 0.52 and 0.169. For the downstream flow the Re and Fr are,

$$\mathrm{Re}_{Zd}(t) = U_d(t)\mathrm{Z}_{44}(t)H/\upsilon \tag{10}$$

$$Fr_{Zd}(t) = U_d(t)/\sqrt{g\mathrm{Z}_{44}(t)H} \tag{11}$$

where, U_d is the mean stream-wise downstream velocity.

Four Kenek wave gauges are used for obtaining the air-water interface elevations at the twelve stream-wise locations at 100Hz frequency (maximum response frequency of 100Hz). Each wave gauge has a thin needle that remains in contact with the free surface throughout the sampling by maintaining a constant needle resistance value in between the free surface and the probe circuitry. The wave gauge has a servo motor that raises and lowers the needle maintaining the measured resistance value while sampling the needle displacement. The maximum range of the wave gauge needle is 30 cm and the maximum response speed is 1200mm/s. The wave gauges are calibrated by varying the water height by known elevations and recording the corresponding voltage values. The non-dimensional air-water interface elevation is,

$$\zeta_j(t) = z_j(t)/H \tag{12}$$

where, the subscript j refers to the x location of the wave gauge. The decomposition of the normalized instantaneous elevation into its mean and fluctuating components is defined as,

$$\zeta_i(t) = Z(t) + \zeta'(t) \tag{13}$$

where ζ' is the fluctuating component and $Z(t)$ is the ensemble averaged mean elevation,

$$\mathrm{Z}(t) = \lim_{N\to\infty} \frac{1}{N} \sum_{i=1}^{N} \zeta_i(t) \tag{14}.$$

The flow rate measurements from the venturimeters were also obtained simultaneously with the upstream PIV and downstream pitot probes. The data acquisition frequency for the transducers (maximum response frequency of 40Hz) connected to the orifice meters are also set at 100 Hz and eight measurements were used similarly to calculate the mean. The total flow rate Q_v is the sum of the flow rates from each venturimeter. The upstream and downstream velocity profiles along with the free surface elevations are also used to calculate the inlet and outlet flow rates. The data reduction equations for estimating the inlet and outlet flow rates are,

$$Q_u(t) = W \cdot U_u(t) \cdot \mathrm{Z}_{-52}(t)H \tag{15}$$

$$Q_d(t) = W \cdot U_d(t) \cdot \mathrm{Z}_{44}(t)H \tag{16}$$

where, Q_u and Q_d are the inlet and exit flow rates respectively, W is the width of the flume.

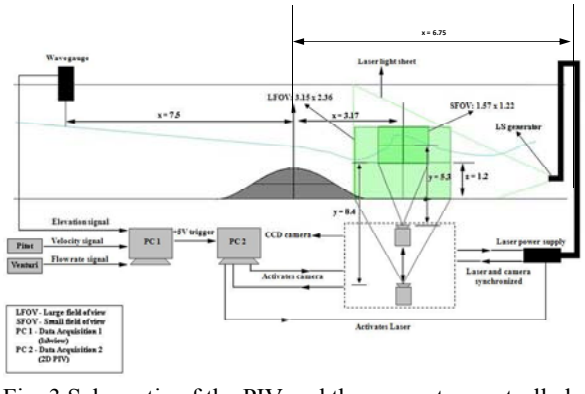

Fig. 3 Schematic of the PIV and the computer controlled data acquisition system

At the breaking wave location immediate downstream

of the bump measurements are obtained at the flume center plane parallel to the stream-wise direction to calculate the overall velocity, vorticity and turbulence flow fields. Fig.3 shows the schematic of the computer controlled data acquisition system and details of the 2D-PIV setup at the breaking wave location and also highlights the PIV measurement areas for large and small fields of view and the camera distances from the flume center plane. Synchronized data acquisition for the wave breaking PIV measurements along with the upstream, downstream and flow rate measurements are facilitated by two trigger mechanisms from two wave gauges. The first wave gauge (not shown in Fig.3) is placed at x = -62 that triggers the data acquisition for the flow conditions. Another wave gauge is placed at x = -7.5 and when the water level at that location drops by ζ = -0.114 the wave gauge sends another trigger signal (5 volt, square sign wave) to PC2 through PC1 for starting the PIV data acquisition at the wave breaking location. While the PIV data is being acquired at PC2, the LabView data is also being acquired at PC1 but at different frequencies. For each wave breaking event, 100 PIV images are recorded at 15 Hz. The data reduction equation for mean vorticity is,

$$\omega_y(t) = \frac{\partial U(t)}{\partial z} - \frac{\partial W(t)}{\partial x} \tag{17}$$

Reynolds stress and turbulent kinetic energy (*TKE*) from 2D-PIV data is also calculated. The two components of Reynolds normal stresses are,

$$\overline{u'(t)^2} = \lim_{N\to\infty} \frac{1}{N} \sum_{i=1}^{N} [u_i(t) - U(t)]^2 \tag{18}$$

$$\overline{w'(t)^2} = \lim_{N\to\infty} \frac{1}{N} \sum_{i=1}^{N} [w_i(t) - W(t)]^2 \tag{19}$$

The Reynolds shear stress is,

$$-\overline{u'w'(t)} = -\lim_{N\to\infty} \frac{1}{N} \sum_{i=1}^{N} [u_i(t) - U(t)][w_i(t) - W(t)] \tag{20}$$

The turbulent kinetic energy for 2D flow measurements can be estimated according to Chang & Liu 1999 as;

$$TKE(t) = \frac{1.33}{2}(\overline{u'(t)^2} + \overline{w'(t)^2}) \tag{21}$$

Convergence studies of the mean velocity and *TKE* is also conducted for both the upstream PIV data and PIV measurements at the breaking wave location. Convergence studies are conducted using the data acquired over the entire velocity vector plot. If N is the total number of times the experiment is repeated then the normalized error in the magnitude of the mean velocities (U and W) at the N^{th} realization are,

$$\delta U_N = \sum_{ij} \left| \overline{U}_N - \overline{U}_{24} \right|^2 / \sum_{ij} \left| \overline{U}_{24} \right|^2 \tag{22}$$

$$\delta W_N = \sum_{ij} \left| \overline{W}_N - \overline{W}_{24} \right|^2 / \sum_{ij} \left| \overline{W}_{24} \right|^2 \tag{23}$$

where, the sum is taken over all the $i \times j$ velocity vectors in the entire vector field. Similarly the corresponding error in *TKE* is,

$$\delta TKE_N = \sum_{ij} \left| \overline{TKE}_N - \overline{TKE}_{24} \right|^2 / \sum_{ij} \left| \overline{TKE}_{24} \right|^2 \tag{24}$$

Static pressure measurements at eight stream-wise locations (x = 2.65, 2.85, 3.05, 3.25, 3.45, 3.65, 3.85 and 4.05) immediate downstream of the bump on the flume floor are obtained for test case L1 only, to calculate the pressure impulses due to the wave breaking. The pressure coefficient is,

$$C_p = (p - p_\infty) / 2\rho \overline{U}_{ub}^2 \tag{25}$$

where, $\overline{U}_{ub}$ is averaged outside the boundary layer and p_∞ is the atmospheric pressure. However, more detailed experiments are necessary to evaluate pressure impulses which will be conducted in future.

2.3 Experimental Repeatability and Uncertainty Analysis

To confirm the repeatability of the wave breaking event wave profiles from different experimental runs were extracted and plotted with respect to the bump location and the mean and standard deviations were calculated. Fig.4 shows the mean wave profiles calculated from 22 runs for different experimental test cases and from CFD. The rectangular box highlighted in the image shows the region within which the highest part of the wave-crest lies. For all test cases the overall average x_b, z_b and t_b values are 3.26 1.88 and 13.12, respectively, and the corresponding percentage standard deviations are 3.42, 4.06 and 4.37, respectively.

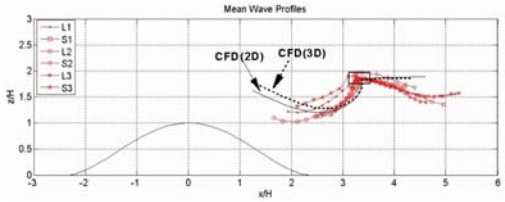

Fig. 4 Mean wave profiles for different test cases (EFD, CFD)

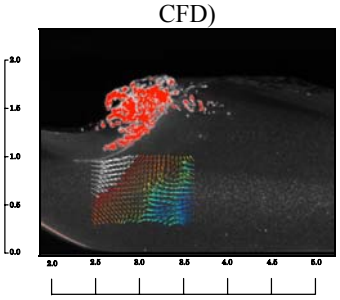

Fig. 5 Example of the vector field under the breaking wave chosen for convergence studies

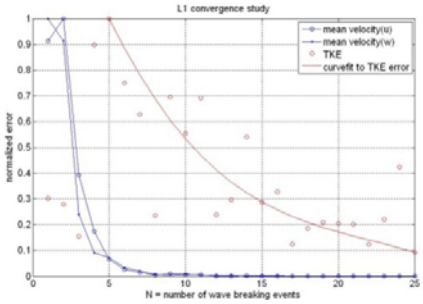

Fig. 6 Convergence plot for L2

For the convergence studies, a rectangular area (cen-

tered at x = 2.72 and z = 0.79) in the most energetic region below the wave breaking region is chosen. Fig.5 shows the area (1.16×0.7) that is chosen for convergence studies under the breaking wave region at time t_b. For all experimental test cases, the normalized errors in mean velocity and *TKE* given by equations (21), (22) and (23) respectively are plotted against the number of repeats of the experiment. Fig.6 shows the convergence plots for L2. Results reveal that for all test cases the normalized error in the mean velocities (U and W components) reduce to less than 5% after 7 successful repeats of the experiment and the *TKE* error reduces to 10% after 22 successful runs. Hence all 2D-PIV measurements in the breaking wave region is ensemble averaged over 22 repeats.

Uncertainty analysis of the wave breaking results follows AIAA standard [14]. The procedures are based on estimates of systematic bias and random precision limits, and their root-sum-square (RSS) combination to ascertain the total uncertainty. Ninety-five percent confidence levels are achieved through careful estimation of bias errors and usage of a large sample, multiple test approach for precision errors.

Table3 Percentage standard deviations

Parameter	% STDEV
ζ at x = -7.5	7.2
Re_{zup}	4.6
Fr_{zup}	4.5
Re_{zd}	3.9
Fr_{zd}	5.9
Q_v (m^3/s)	9.3
Mean velocity U (m/s)	3.8
TKE (m^2/s)	2.9

Uncertainties in the wave breaking measurements are calculated for some of the important parameters. Three sets of overall measurements are obtained for all the above variables and precision limits are calculated from their standard deviations. The bias limit analysis is still in the process of evaluation. Table 3 summarizes the percentage standard deviations of the most important variables at t_b.

3 Computational Methods

CFDShip-Iowa version 6, a Cartesian grid solver for the large-eddy simulation (LES) of two-phase incompressible flows recently developed at IIHR, is used in the current study. This solver is based on the work of Yang and Balaras [15], in which a sharp interface immersed boundary method has been developed to handle complex immersed stationary/moving boundaries on Cartesian grids, and has been extensively expanded to fit the need of ship hydrodynamics applications. A Spalart-Allmaras turbulence model has been added for unsteady RANS simulation. A high-order level set method is used to track the fluid/fluid interface and a sharp interface method (ghost fluid method) is adopted for the treatment of interface jump conditions. In addition, improved particle set and volume-of-fluid methods are developed respectively to couple with the level set method for better volume conservation properties. Various upwind convection schemes including QUICK and WENO have been implemented. High Performance Computing (HPC) components include scalable iterative (multigrid) solvers for the pressure Poisson equation, a parallel tridiagonal system solver for the inversion of momentum equations, and parallel I/O, etc. A summary of the computational methods is presented here; details and references are given in Yang and Stern [8, 9].

3.1 Mathematical Model

3.1.1 Navier-Stokes Equations

Incompressible viscous flows of two immiscible fluids, e.g., air and water, are governed by the Navier-Stokes equations:

$$\frac{\partial \mathbf{u}}{\partial t} + \mathbf{u}\cdot\nabla\mathbf{u} = \frac{1}{\rho}\nabla\cdot\left(-p\mathbf{I}+\mathbf{T}\right)+\mathbf{g} \tag{26}$$

$$\nabla\cdot\mathbf{u} = 0 \tag{27}$$

where t is the time, $\mathbf{u}$ is the velocity vector, p is the pressure, $\boldsymbol{I}$ is the unit diagonal tensor, ρ is the density, $\mathbf{g}$ represents the gravity acceleration, and $\mathbf{T}$ is the viscous stress tensor defined as

$$\mathbf{T} = 2\mu\mathbf{S} \tag{28}$$

with μ the dynamic viscosity and $\mathbf{S}$ the strain rate

$$\mathbf{S} = \frac{1}{2}\left[\nabla\mathbf{u}+\left(\nabla\mathbf{u}\right)^T\right] \tag{29}$$

where the superscript T represents transpose operation.

The governing equations can be non-dimensionalized by normalizing each quantity above by the reference velocity and length scales of the problems considered and will not be presented here. The dimensionless parameters such as the *Re*, *Fr*, and Weber numbers are defined with the physical properties of the phase of interest, i.e., water in the current study.

3.1.2 Interface Modeling

Defining the interface Γ as the zero level set of a signed distance function ϕ, or the level set function, the position of the interface can be tracked by solving the level set evolution equation

$$\frac{\partial \phi}{\partial t} + \mathbf{u}\cdot\nabla\phi = 0 \tag{30}$$

Each phase of constant density and viscosity can be defined by the level set function in the computational domain and sharp jumps of the fluid properties occur at the phase interface. In this paper, the density keeps its sharp jump and the viscosity is smoothed over a transition band across the interface,

$$\begin{aligned}\rho &= \rho_G + \left(\rho_L-\rho_G\right)H\left(\phi\right)\\ \mu &= \mu_G + \left(\mu_L-\mu_G\right)H_\varepsilon\left(\phi\right)\end{aligned} \tag{31}$$

where, the subscripts G and L represent gas and liquid phase, respectively, the stepwise Heaviside function is,

$$H\left(\phi\right) = \begin{cases}1 & \text{if} \quad \phi \ge 0\\ 0 & \text{if} \quad \phi < 0\end{cases} \tag{32}$$

and, the smoothed Heaviside function is,

$$H_\varepsilon(\phi)=\begin{cases}1 & \text{if} \quad \phi>\varepsilon \\ \frac{1}{2}\left[1+\frac{\phi}{\varepsilon}+\frac{1}{\pi}\sin\left(\frac{\pi\phi}{\varepsilon}\right)\right] & \text{if} \quad |\phi|\le\varepsilon \\ 0 & \text{if} \quad \phi<-\varepsilon\end{cases} \tag{33}$$

Since the fluids considered here are viscous and no phase change occurred, the velocity across the interface Γ is continuous:

$$[\mathbf{u}]=0 \tag{34}$$

where, [ ] indicates the jump at the interface, i.e., $f_L^I - f_G^I$ for a variable f with superscript I denotes interface. The exact jump condition for stress is

$$\left[\mathbf{n}\cdot\left(-p\mathbf{I}+\mu\left(\nabla\mathbf{u}+(\nabla\mathbf{u})^T\right)\right)\cdot\mathbf{n}\right]=\sigma\kappa \tag{35}$$

where, $\mathbf{n}$ is the unit vector normal to the interface σ is the coefficient of surface tension, and κ is the local curvature of the interface. With a smoothed viscosity and continuous velocity field, the stress jump condition reduces to

$$[p]=p_L^I-p_G^I=-\sigma\kappa \tag{36}$$

As will be discussed later, the surface tension effect is neglected in the present study.

3.1.3 Turbulence Modeling

In the LES approach, the Navier-Stokes equations are spatially filtered such that the large, energy carrying eddies are resolved and the small scale, dissipative eddies are modeled by a sub-grid scale stress model. The deviatoric part of the subgrid-scale (SGS) stress tensor, $\bar{\tau}=\overline{\mathbf{uu}}-\bar{\mathbf{u}}\bar{\mathbf{u}}$, is parametrized following the Smagorinsky procedure as:

$$\bar{\tau}-\frac{1}{3}\mathrm{trace}(\bar{\tau})\mathbf{I}=-2\nu_t\bar{\mathbf{S}} \tag{37}$$

and the turbulent eddy viscosity is defined as

$$\nu_t=C\Delta^2|\bar{\mathbf{S}}|, \quad \text{and} \quad |\bar{\mathbf{S}}|=\sqrt{2\bar{\mathbf{S}}\cdot\bar{\mathbf{S}}} \tag{38}$$

The model parameter C in the eddy viscosity definition has to be determined to close the equations. In this paper the Lagrangian dynamic SGS model is chosen as it can handle complex geometries without the requirement of homogeneous direction(s).

On the other hand, in the unsteady RANS approaches, the Reynolds stresses, $\tau'=-\overline{\mathbf{u}'\mathbf{u}'}$, appear in the governing equations as a result of the Reynolds averaging and are modeled by the Boussinesq eddy viscosity model

$$\tau'-\frac{1}{3}\mathrm{trace}(\tau')\mathbf{I}=2\nu_t\bar{\mathbf{S}} \tag{39}$$

where the bar and prime operators above are given by the Reynolds averaging procedure. The eddy viscosity is given by the Spalart-Allmaras one equation turbulence model, which is omitted here.

3.2 Numerical Method

3.2.1 Navier-Stokes Solver

The finite differences method is used to discretize the Navier-Stokes equations on a non-uniform staggered Cartesian grid, in which the velocity components u, v, and w are defined at centers of cell faces in the x, y, and z directions, respectively, and all other variables, i.e. p, ϕ, ρ, μ, and ν_t are defined at cell centers. A semi-implicit time-advancement scheme is adopted to integrate the momentum equations with the second-order Crank-Nicolson scheme for the diagonal viscous terms and the second-order Adams-Bashforth scheme for the convective terms and other viscous terms. A four-step fractional-step method is employed for velocity-pressure coupling, in which a pressure Poisson equation is solved to enforce the continuity equation:

1. Predictor:
$$\frac{\hat{u}_i-u_i^n}{\Delta t}=\frac{1}{2}\left(3A_i^n-A_i^{n-1}\right)+\frac{1}{2}\left(C_i^{n+1}+C_i^n\right)-\mathrm{Grad}_i\left(p^n\right), \tag{40}$$
2. First Corrector:
$$\frac{u_i^*-\hat{u}_i}{\Delta t}=\mathrm{Grad}_i\left(p^n\right), \tag{41}$$
3. Pressure Poisson Equation:
$$\frac{\partial}{\partial x_i}\mathrm{Grad}_i\left(p^{n+1}\right)=\frac{1}{\Delta t}\frac{\partial u_i^*}{\partial x_i}, \tag{42}$$
4. Second Corrector:
$$\frac{u_i^{n+1}-u_i^*}{\Delta t}=-\mathrm{Grad}_i\left(p^{n+1}\right), \tag{43}$$

where superscript n denotes time step, subscript i = 1, 2, 3 represents i-coordinate, A and C denote terms treated by the Adams-Bashforth and Crank-Nicolson schemes, $\hat{u}_i$ and u_i^* are the first and second intermediate velocities, respectively. $\mathrm{Grad}_i(p)$ is a pressure gradient term defined at the center of the cell faces (collocated with velocity components) with the jump conditions incorporated in it. For instance, in the x direction,

$$\mathrm{Grad}_i\left(p\right)_{i+1/2}=\frac{1}{\rho_{i+1/2}}\frac{\left(p_{i+1}-p_i\right)+\sigma\kappa^I}{\Delta x} \tag{44}$$

where the cell face density is defined as in the ghost fluid method with the sharp jump condition at the interface considered utilizing the level set function.

In Eq. (40) the convective terms are discretized using a third-order QUICK and higher-order WENO schemes are available. All other terms are discretized with the standard second-order central difference scheme. Eq. (40) is approximated with the approximate factorization method. A parallel tridiagonal system solver and a multigrid solver are used to inverse the momentum and pressure Poisson equations, respectively.

3.2.2 Interface Tracking

The level set and the reinitialization equations are solved using a third-order TVD Runge-Kutta scheme for time advancement and the fifth-order HJ-WENO scheme for spatial discretization. The solution time of these equations does not pose a significant overhead as they are solved in a narrow band several grid-cells wide.

Although the level set (LS) method has many advantages comparing to other interface tracking/capturing methods, it suffers from numerical dissipation and usually

comes with volume loss in the under-resolved regions. Two different approaches are used to improve the volume conservation properties of the LS method: one is a particle set method and the other is a volume-of-fluid method. A hybrid particle level set (PLS) method can be developed by combining the former with the standard LS method. The particles placed around the interface follow the motion of the interface and carry information about the position and interface, which can be used to correct the level set function to be the distance function of the interface. A generalized particle reseeding strategy is developed instead of using the original strongly problem-dependent method in Enright *et al.* [16]. On the other hand, in the latter, volume conservation is imposed directly by solve the volume fraction transport equation. In a coupled level set and volume-of-fluid (CLSVOF) method such as Sussman and Puckett [17], the interface is reconstructed based on the volume-of-fluid (VOF) function with the interface normal computed from the level set function. The level set field is then reset to reflect the position of the reconstructed interface, which satisfies the volume conservation constraint. In the present study, the piecewise linear interface construction (PLIC) scheme for the VOF method presented by Gueyffier *et al.* [18] is improved to be second-order in time and used on non-uniform grids. Also, a very efficient re-distance algorithm has been developed.

3.2.3 Immersed Boundary Treatment

A sharp interface immersed boundary method is adopted here to treat the immersed boundaries/bodies in a non-uniform Cartesian grid. In this approach, the grid generation for complex geometries is trivial since the requirement that the grid points coincide with the boundary, which is imperative for body-fitted methods, is relaxed; while the solution near the immersed boundary is reconstructed using momentum forcing in a sharp-interface manner.

To summarize, the first step is to establish the grid-interface relation with a given immersed boundary description, such as parametrized curve/surface or a triangulation. In this step all Cartesian grid nodes are split into three categories: (1): fluid-points, which are points in the fluid phase; (2) forcing points, which are grid points in the fluid phase with one or more neighboring points in the solid phase; (3) solid-points, which are points in the solid phase. The Navier-Stokes solver described in the previous section is applied on all points of the Eulerian grid as if the fluid/solid interface was not present. The effect of the immersed boundary on the flow is introduced through the discrete forcing function, which is computed only at the forcing points by directly enforcing the boundary conditions. In general, the velocity at the forcing points can be computed by means of linear interpolation that involves the projection of the forcing point on the interface and two points in the fluid phase.

3.3 Software Architecture and HPC

One of the major objectives of the development of CFDShip-Iowa version 6 is to make use of the on-coming petascale computers and provide fast turnaround for simulation-based design in ship hydrodynamics. Efficiency and sustainable development of the solver are among the major considerations in the software design. Modern programming language Fortran 95 is chosen and a modulized approach is followed for the code development.

The simple topologic structure of Cartesian grids is favorable for coarse-grain parallelization. The parallelization is done via a domain decomposition technique using the MPI library. A simple domain decomposition technique is used in CFDShip-Iowa version 6 where the Cartesian grid is divided into uniform pieces, each of which resides in one processor. Optimal load balance can be achieved except for a small amount of overhead due to interface and immersed boundary treatment, which may be unevenly distributed over processors.

A parallel tri-diagonal system solver is used with the approximate factorization of momentum equations, no iterations are needed for the inversion of the momentum equations. For the pressure Poisson equation, a highly efficient, scalable multigrid-preconditioned Krylov subspace solver from PETSc has been included in the code. Usually, the Poisson solver takes most of the CPU time in a single time step.

Parallel I/O based on MPI 2 is implemented. Instead of the usual approaches that one process collects all data from all processes and write to one file, or, each process write its data to its own file, in the current approach all processes write its data to one single file, which is highly scalable and can greatly simplify the I/O operation and minimize the post-processing overhead.

4. Computational Setup and Tests

The 2D simulations are conducted on a computational domain of x = [-52, 44] and z = [0, 5], with a grid size of 768 × 256. The boundary conditions are given in Fig.7. The inlet velocity imposed at the left boundary is 0.87 *m/s* for water and zero for air. The initial free surface elevation is ζ = 1.85 and a uniform velocity field of 0.87 *m/s* is prescribed in the water domain at t=0 with the air phase at rest. The corresponding *Re* is 99441 and *Fr* is 0.82. The initial velocity and free surface elevation are chosen based on the sensitivity study discussed in the following. The experimental flow conditions, as shown in Fig. 10, will be used in the future investigations. The time step initially is 5×10^{-5} and then is reduced to 1×10^{-5} after the flow gets violent due to wave breaking. 3D Large Eddy Simulation (LES) is also performed with a spanwise size of 0.4l (l = 0.2758 *m*, bump length) in the y direction. Some preliminary results of the 3D simulation are presented in this study, more detailed investigation and discussions will be provided in the future work.

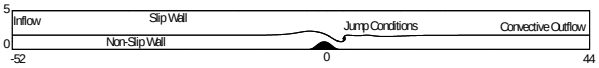

Fig. 7 Computational domain

The breaking point position is sensitive to the initial water height and inlet velocity. Tests are carried out to investigate the effects of impulsive inlet velocity and water height on the wave breaking position. As shown in Table 4,

with the same water height, the increase of the inlet velocity tends to move the x position to the downstream from the bump, while the z position is not affected much. Table 5 shows that both the x and z coordinates increase with water height when the inlet velocity is fixed. With an inlet velocity of 0.87 m/s and water height of 1.85, the wave breaking occurs at (3.28, 1.83) which is quite close to the experimental measurement (3.2, 1.8). This velocity and water height are then chosen as the initial conditions for the computations.

Table 4 Inlet velocity effect on the wave breaking position

Water Height	Velocity (m/s)	x_b	z_b
1.67	0.38	1.77	1.63
1.67	0.76	2.80	1.61
1.67	0.87	3.06	1.60
2.00	0.76	3.15	2.01
2.00	0.87	3.52	2.01
2.00	1.14	4.57	2.04

Table 5 Water height effect on the wave breaking position with same inlet velocity

Velocity (m/s)	Water Height	x_b	z_b
0.87	1.67	3.06	1.60
0.87	1.75	3.15	1.67
0.87	1.85	3.28	1.83
0.87	2.00	3.52	2.01

Calculations are performed on three different grids with consecutively reduced (by a factor of $\sqrt{2}$) sizes from 1088 × 352 to 768 × 256 and 544 × 176 for grid sensitivity study. Computational results (jet overturning) on the three grids are shown in Fig. 8. The overall structures of the interface obtained on the three grids are very similar. The jet tip is much thinner and sharper on a fine grid than on a coarse grid since a fine grid can capture more details of the interface structure with higher grid resolutions. Fig. 8 also indicates that the jet angle with respect to the horizontal surface decreases with grid refinement. It can also be found that the angle on the medium grid is closer to that on the fine grid than on the coarse grid as indicated in Figs. 8a, b and c, except in Fig. 8d where the tip of the jet on the fine grid breaks up. Only a qualitative grid convergence analysis is made here, a quantitative verification of iterative, time step and grid convergence is necessary in the future work. Although much smaller interface structures can be resolved with higher grid resolutions, the overall large scale dynamics of wave breakings are not affected by the small interface structures. The grid with a medium size is used in the following simulations for 2D cases. For 3D computations, 32 uniform grid points are used in the y direction with the same grid sizes in both x and z directions as in a 2D case.

As previously mentioned, surface tension is not considered in the present study. Although the small scale interface structures will be affected by the surface tension force, its effect on the major wave breaking events is not significant. Based on the inlet velocity and bump height, the Weber number ($We=\rho U^2 H/\sigma$) is 11.88, which is large enough to neglect the capillary effect on the large scale interface structures. For the future 3D simulations, surface tension effect will be included in order to properly capture small scale water droplets and air bubbles.

For comparison purposes, the LS, PLS, CLSVOF methods are used for the calculations. The time sequences of wave breaking process computed using the three different methods are given in Fig. 9. As will be discussed later, the major events in the wave breaking process are maximum wave height, first plunge, oblique splash, vertical jet, repeated processes, chaotic motions and broken wave swept downstream. At the early stage of the computations, the general structures of the wave profile are very similar. The maximum wave height (frame 1) and the first jet plunge (frame 2) are well demonstrated in all the three methods. After the jet hits the trough surface (frame 3), an oblique splash-up with many small droplets can be found in the CLSVOF method, this is in agreement with the experimental findings. As for the LS and PLS methods, the oblique splash-up is not properly captured. The vertical jet reaches its maximum height (frame 4), which can be seen in all the three methods. In the subsequent events (frame 5-8), the CLSVOF method shows the second plunge, oblique splash-ups and vertical jet, and the third plunge at last. In both the LS and PLS methods, however, only the second jet plunge is indicated after which the flow appears to enter a chaotic motion of air and water.

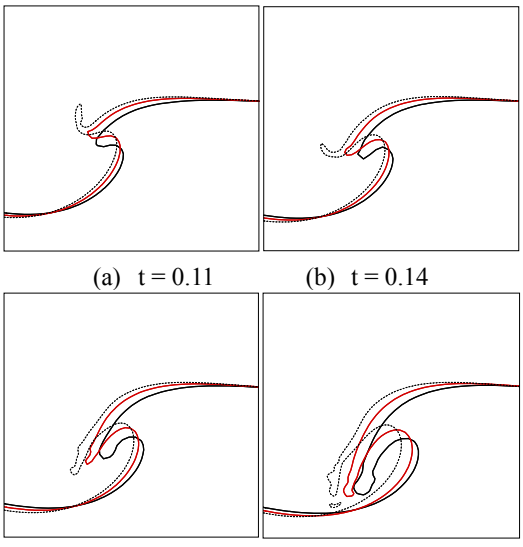

Fig. 8 Comparison of three different grids: coarse grid (black solid line), medium grid (red solid line), fine grid (black dotted line)

Moreover, in the entire wave breaking process, small scale droplets and air bubbles can hardly be found in the LS method, this is because the LS method tends to smooth out the sharp edges of the interface due to its inherent mass loss property. As for the PLS method, more fine structures of the interface have been captured than the LS method.

The CLSVOF method may be the best among the three interface modeling methods with an improved mass conservation property and providing more realistic and reasonable simulation results for the wave breaking phenomenon. Therefore, in the following simulations, only the CLSVOF results are presented.

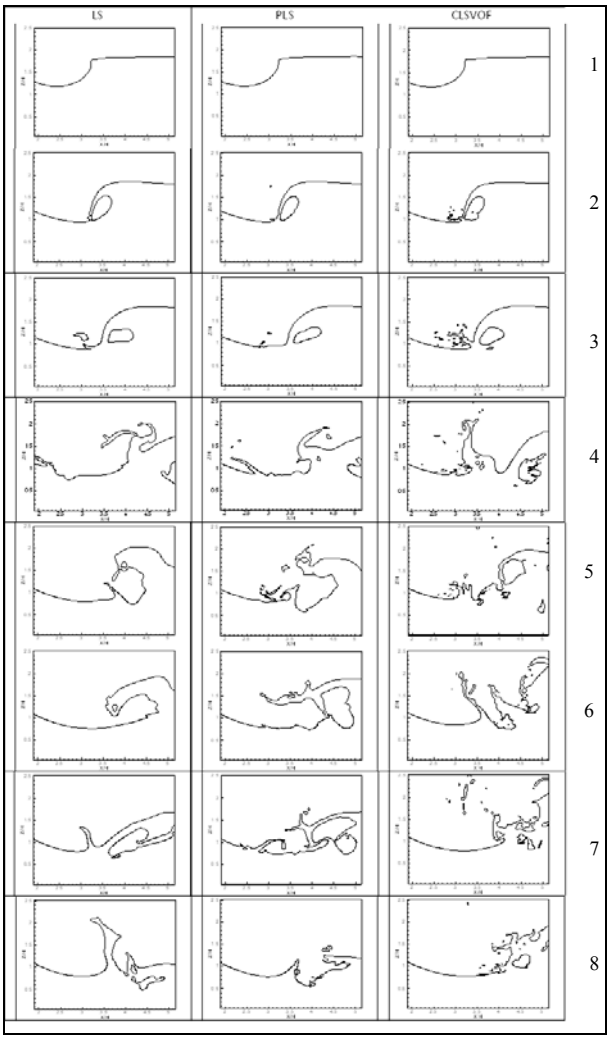

Fig. 9 Comparison of three different interface tracking methods. Left: LS; middle: PLS; right: CLSVOF.

5 Overall Description of EFD Flume Flow and Wave Breaking

After the pumps are switched on, the downstream flow starts moving first at t = -8 seconds (Fig.10a) and at t = -4 seconds the upstream flow starts moving as well. During the acceleration the water level in the downstream side keeps lowering while in the upstream side it first goes down and then goes up due to a travelling wave that starts propagating downstream from the inlet reservoir. The wave breaks at t = 0. The PIV data acquisition for L or S test cases starts at t = -1.3 seconds and continues till t = 1.6 seconds. After t = 1.6 seconds the broken wave is swept downstream and eventually a hydraulic jump forms at x = 20 at t = 2 seconds. On the whole, data is acquired for the flow conditions in between t = -13.4 and t = 6.6 at 100Hz and data for PIV is acquired in between t = -1.3 and t = 1.6 at 15Hz. Once the data acquisition is over the pumps are switched off.

The overall flow conditions are summarized in Fig.10. Fig.10a shows the time series of the mean upstream and downstream *Re* and *Fr*. The delayed movement of the upstream flow is expected since the downstream side is the suction side of the pumps. Fig.10b shows that the upstream flow remains subcritical, $Fr_{Zu} < 1$ during the entire wave breaking event while the downstream side it becomes super-critical after t = -1.

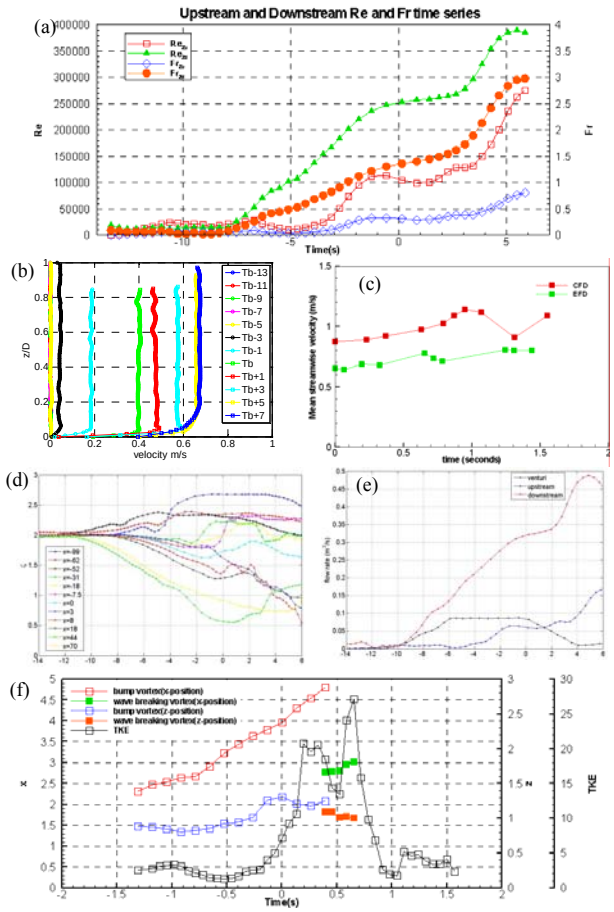

Fig. 10 Experimental flow conditions. (a) Time series of upstream and downstream Reynolds and Froude numbers. (b) Mean upstream velocity profiles at different time steps. (c) Time series of mean stream-wise velocity. (d) Time series of wave elevations. (e) Time series of flow rates. (f) Vortex paths and *TKE* time series. *TKE* is non-dimensionalized by $\overline{U}_{ub}^2$

Fig.10b shows the mean upstream velocity profiles at different time steps for test case V1. The velocity profiles show that at t = -2 the mean profile resembles laminar flow, at t = -1 the flow is in the transitional regime and at t = 0 the mean profile looks turbulent. Mean velocity profiles show an overshoot near the flume bottom boundary for

most time steps until t = 4 seconds as expected in a suddenly accelerated flow. According to He & Jackson [19] in a transient flow the bulk fluid responds slower to the fluid acceleration compared to the boundary layer that causes this overshoot in the velocity profile. The upstream and downstream flow accelerations for the present flow are 0.07m/s^2 and 0.13m/s^2 respectively as compared to [19] whose accelerations ranged from 0.075 – 0.378. The mean stream-wise upstream velocity at t = 0 is calculated to be 0.39 m/s and this value is used as the reference upstream velocity. Fig 10c shows the time series of the subtracted mean $\overline{U}$ values where, $\overline{U}$ is the mean over x and z at each time step. The experimental mean velocity is about 20% lower than the computational one.

Fig.10d shows the mean time series of the air-water interface elevations at different stream-wise locations. The travelling wave was first noticed from visual observations. Air-water interface elevation measurements showed evidence of this water front that was detected by a sharp rise in the wave elevation at any stream-wise location where it had just reached. Fig.10d shows the sharp rise at t =-4.8 seconds at x = -99. As the wave travels downstream the sharp rise can also be observed all the way until x = -7.5. The mean speed of the wave front is estimated to be 2.58 m/s which is approximately 6.6 times greater than $\overline{U}_{ub}$ as it travels from x = -99 to -7.5. Eventually at a later time t = 6 seconds, a hydraulic jump is formed at x = 20. This can be seen in the sharp rise of the air-water interface elevation in between t = 0 and 6 at x = 18, 44 and 70.

Fig.10e shows the comparison of the time series of the mean upstream and downstream flow rates with venturimeter flow rates. The downstream flow rate is higher than the upstream one as expected (due to the pump suction) and all the three flow rate show different values and trends. The venturimeter flow rate first ramps up and stays steady at approximately 0.085 m^3/s for 6 six seconds in between t_b-6 and t_b and then eventually reduces after the wave has broken. The reduction of the flow rate in the venturimeters after staying steady for six seconds is unexpected, since both the upstream and downstream flow rates in the flume keep increasing even after t_b. As the flow accelerates in the channel the water level keeps reducing all along its length. However, the end reservoir at the downstream side is where the water level reduces most and during the course of the breaking the low water level in the reservoir reduces to such an extent that air gets entrapped in it which chokes the pipe lines below the flume. This is the reason why the flow rate reduces in the pipes after the plateau but keeps increasing in the channel.

Fig.10f shows the time series of the mean *TKE* calculated within a rectangular region (Fig.5) below the breaking wave. Fig.10f also shows the locus of the two main vortical structures (bump vortex and wave breaking vortex) that are generated downstream of the bump. Details of *TKE* and vorticity will be discussed in section 7.

6 Wave Breaking Process

The plunging wave breaking process has been characterized in the previous studies by four major phases including steep wave formation, jet formation and overturning, splash-up and air entrainment as discussed in [1-3]. The plunging wave breaking processes discussed in the above studies are summarized in Table 1 along with the present EFD and CFD results. The first two phases, i.e., steep wave formation and jet overturning, are very similar in most experimental and numerical studies even though the flow conditions and the mechanism that induces wave breaking are different. However, the subsequent phenomena after the jet overturning observed in the above studies vary considerably. The angle of the overturning jet just prior to the plunge varies with different studies, while the surface profile beneath the jet is approximated with the similar elliptical shape. After the jet hits the trough surface, the splash-up angles are different for different studies, and different researchers have different opinions about the origin of the splash-ups. Most of the previous studies have reported occurrence of successive splash-up cycles with reduced energy after the first plunge and the degeneration of the flow into a chaotic motion.

Herein, wave breaking is triggered by the flow over a submerged bump which differs significantly from the previously mentioned experimental studies in flow conditions, jet overturning directions and subsequent events. The following major events in the plunging wave breaking process have been identified: maximum wave height, first plunge, oblique splash, vertical jet, two repeated processes, chaotic motions and broken wave swept downstream. Fig.11 summarizes the overall PIV results in the wave breaking region for test case L2 and its comparison with CFD at various time steps that describe the most important events in the wave breaking process as listed in Table 1. Results from the close-up views of the breaking wave (test case S1) are presented in Fig.12 for the first four time steps only. Fig.12 has the same arrangement of columns as Fig.11. Video images of the plunging breaker with reference scales and PIV images with overlaid CFD air-water interface profiles are presented in column 1 and 2 respectively. The CFD t_b time is 0.49 seconds. The EFD tb times have already been mentioned in section 2.2. Time t = 0 refers to t_b according to equation (3). The CFD air-water interface profiles were initially studied to identify the overall wave breaking process and its major events. Subsequently, those events were also identified qualitatively from the video and PIV images in EFD. In the current layout of Fig.11 and 12 the EFD and CFD results are compared side by side for those particular events and hence the time instances do not necessarily match due to the differences in the initial conditions. Although the CFD time is given in the CFD U contour plot, unless otherwise specified, the EFD time is always referred to in the discussions.

At time t = 0 the wave crest becomes steepest when it reaches its maximum height. As shown in Fig.4, although the CFD and EFD wave breakers are located at almost the same place, the wave profiles are quite different. The wave height and wave steepness are given in Table 1. The wave height (η) is defined as the vertical distance from the bottom of the trough to the crest, and the wave steepness is defined as $ak = \eta\pi / \lambda$, where λ is the wave length. As

shown in the table, both the CFD and EFD *ak* values are much larger than that of the experimental study by Bonmarin [2]. Moreover, the wave breaks in the opposite direction to the mean flow, which is one of the major differences from the previous experimental studies.

As the wave crest starts to overturn the steep angle θ_E, defined as the angle between the horizontal free surface and the jet's longitudinal axis, also increases, and its edge breaks into some small droplets in air. At the instant just prior to the first plunge, the CFD steep angle is approximately 50 degrees which is less than the EFD value but matches [3]. At t = 0.065, the first plunge occurs when the overturning jet impinges onto the free surface of the trough. The θ_E increases to approximately 75 and 85 degrees in the CFD and EFD profiles, respectively compared to the previous time step. With the overturning jet, a large amount of air below the jet is entrapped which forms a big air bubble. The entrapped air bubble can also be observed in the close up PIV image at t = 0.065. The size of the air bubble in CFD is almost 1.5 times larger than the EFD. The CFD results show that the entrapped air bubble initially resembles an ellipse with an axis ratio of 2.153 which is slightly larger than those (usually, √3) found in the EFD and previous studies.

Once the jet tip touches the trough surface, splash-up initiates and develops at the location where the jet impacts. At t = 0.196 as shown in CFD plot, an oblique splash-up is generated towards the upstream direction with a spray region. This spray region is more clearly shown in the experimental video image. The PIV image also shows that the red (the color indicates bubble concentration) region intensifies as can be seen from the magnified view. The splash-up angle differs from [3] in which the splash-up is initially vertical and then becomes oblique towards the original wave crest. The observations of the present study are close to those reported by [1] and [2]. This oblique splash-up appears to "rebound" from the overturning jet rather than originates from the trough surface, which can be clearly seen from the CFD velocity vector field. The origin of the oblique splash-up is also indicated in Fig. 13c which shows the 3D wave profile.

The splash-up intensifies and a vertical jet can be clearly observed in the CFD profiles with its maximum height of ζ = 2.15 at t = 0.327. The video image shows the spray zone grows in size with more intense splash-up reaching a maximum height of ζ = 2.22. In between x = 2.2 and x = 4.6 the broken wave creates an aerated region. A vertical jet can also be observed at x = 3.05 that is ejected from the trough. The CFD velocity vector field shows that the fluid of vertical jet mainly comes from the disturbed trough surface, which can also be seen from the 3D wave profile in Fig.13e. After the first wave plunge, the splash-up initially originates from the plunging crest which forms an oblique spray and intensifies with more water coming from the trough. This agrees with the explanation of [3] on the origin of the splash-ups. The initially entrapped air bubble eventually breaks up at around t = 0.392 (not shown here). Severe bubble shape deformations can be seen in the CFD plot as it moves downstream.

As the vertical jet decreases in height, another jet is formed which starts to initiate the second plunge. As clearly shown in the CFD U contours plot (refer to the CFD time), at t = 0.79, the second plunge occurs. At this time, the initially entrapped air bubble has been swept downstream. The second oblique splash-ups can be found in the CFD results at t = 0.87 and the second vertical jet is formed at t = 0.95. At t = 1.07, the third jet impacts onto the trough surface. After that, multiple small scale splash-ups and plunges keep occurring. In EFD, since the impact region is highly aerated the subsequent events are not as clearly seen as in the CFD. The EFD results show that the second plunge occurs at t = 0.653 and the second oblique splash-up occurs at t = 0.719. Ejections of small volumes of fluids can be seen at x = 2.6 and 2.75 in the PIV image. At t = 0.784 a small vertical jet can be observed from the video image at x = 3.35. At t = 1.242 the splash-up from the previous event plunges for the third time towards the bulk fluid. This is referred to as the third plunge. At t = 1.307 chaotic repeats of plunging and splash-ups occur and at t = 1.438 the wave is swept downstream leaving a trail of aerated region.

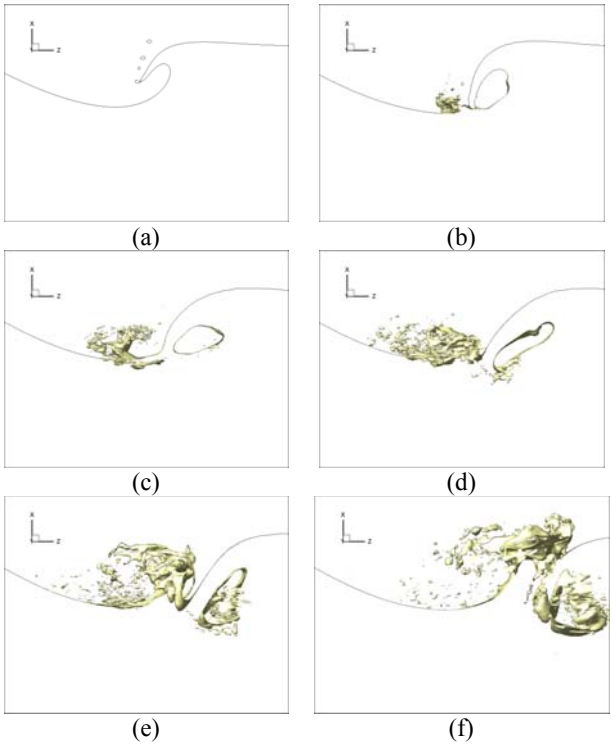

Fig. 13 3D instantaneous free surface profiles of wave breaking process.

The CFD profiles show that the wave breaking occurs further downstream compared to the EFD profiles, which is clearly seen in the first and second plunging events. This is likely because the initial mean flow velocity is higher in the CFD simulations. It is found that the entrapped air bubble after the first plunge collapses in EFD, but remains intact in CFD. This may be because of 3D instability, which can

contribute to the relatively short life of the air bubble [1] that does not exist in the 2D simulations. A clear two-phase (aerated) region is demonstrated in the experimental video images after the jet overturning. However, it is hard to define an exact two-phase region for the 2D simulations. Some preliminary results of the 3D LES are shown in Fig.13. As compared to the 2D case, more splash-ups can be observed, and the region of spray is well defined. The entrapped air bubble undergoes serious shape deformations and eventually collapses due to the 3D instabilities. Since the interface is modeled via an interface tracking method which is not able to capture air bubbles or droplets at the scale less than the grid spacing, a mixture model is needed in order to properly simulate the aerated region in future investigations.

7 Velocity, Vorticity, Turbulence and Air Flow Fields

The third and fourth columns of Fig.11 show the EFD U contours and the CFD U contours, respectively at the time steps that correspond to the wave breaking process with the velocity vectors overlaid on top. The fifth column shows the EFD *TKE* contours at the same time steps. All contour plots and velocity vectors are presented in dimensional form. All EFD data is ensemble averaged and CFD data is instantaneous. To visualize the vortical structures more distinctly, the mean stream-wise velocity component within the water phase of the display area at each time step has been subtracted from the vector fields for both EFD and CFD. To be consistent with the vector representation the mean stream-wise velocity has also been subtracted from the background contours. Fig 10c shows the subtracted mean $\overline{U}$ values at each time step and hence, ΔU ($\Delta U = U - \overline{U}$ where, $\overline{U}$ is the mean over x and z at each time step) instead of U is presented here. The CFD velocity vectors of column 4 are of the same magnitude as the EFD vectors of column 2 and not the vectors in column 3 whereas, the EFD velocity contours in column 3 are of the same scales as the CFD velocity contours of column 4. Even though the CFD simulations were conducted for a much larger domain size, in the present layout the CFD x and z limits are matched with the EFD scales for comparison.

At t = -1.307, EFD ΔU contours (not presented for t = -1.307) show two distinct regions of positive and negative ΔU above and behind the bump, respectively, in between x = 2 and x = 3 due to the presence of the bump vortex. In between $-1.307 \leq t \leq 0$, the positive ΔU region extends downstream with its magnitude increased in a layer from the free surface to Δz = 0.75. At time t = 0, the positive region extends beyond x = 5.15 with the magnitude reduced in the region where steep wave is formed. A negative ΔU region in the crest initiates and intensifies after the first plunge. In between $0 \leq t \leq 1.438$, the positive ΔU region moves towards the bottom with the magnitudes continuing to increase. For $0 \leq t \leq 0.327$, the S1 results show resolvable details of steep wave formation, first plunge, oblique splash and the vertical jet. For $t < 0$, due to the differences in the impulsive start conditions, CFD ΔU contours are different from EFD. For $t \geq 0$, similar flow trends can be found in CFD ΔU contours, with more detailed resolutions of plunging, splashing, vertical jet and bubble entrainment events in the wave breaking region.

Trends for the mean vertical velocity were determined from the W contours (not shown here) but can also be deduced from the velocity vectors. At t = -1.307, a positive and negative W region are observed behind the bump and downstream of the bump, respectively, that extend to x =3, again due to the presence of the bump vortex. For $-1.307 \leq t \leq 0$, a positive W region starts to form and increases in magnitude in the crest, and reaches the maximum before t = 0. After t = 0.065, the negative W region behind and above the bump intensifies with its magnitude increased, while the region of positive W in the crest decreases in magnitude as the crest falls. In between $0 \leq t \leq 0.327$, high vertical velocities can be observed near the trough region in between x = 2.5 and 3.5 in between t = 0 and 0.327 which is due to the rising fluid as the wave grows and reaches max height. At t = 1.438, a very strong negative W region can be observed behind the bump. At t = 0.065 Fig.12 shows the overturning jet impinging on the trough. The downward jet velocity (w_j) is calculated to be 0.17 times the mean upstream velocity ($\overline{U}_{ub}$) at t = 0. Again, the CFD W vectors show similar flow trends as the EFD. In the wave breaking region, more detailed information of plunging, splashing, and vertical jets and entrapped bubbles can be found.

Initially at t = -1.307 seconds (not shown here), a clockwise rotating span-wise vortex with center at (2.125, 0.9) is shed from the bump much earlier and is convected in the vertical direction by the rising fluid and also in the downstream direction by the mean flow. The strength of this bump vortex is $12s^{-1}$ with its center at (x, z) = (2.125, 0.9). The bump vortex is approximately 1.5 in diameter. The path of this bump vortex which, is shed only once during the entire wave breaking process is shown in Fig.10f. It travels from x = 2.3 to x = 4.8 and z = 0.9 to z = 1.2 within t = -1.308 and t = 0.457. However, it is quite clear that by the time the wave plunges (t = 0.065 seconds) the bump vortex has already been swept downstream of the breaking region under the crest. At t = 0.196 the aerated region under the broken wave starts to grow and at t = 0.327 the growth of the wave breaking vortex can be clearly seen from the velocity vectors. This vortex slowly moves downstream for the next whole second, the locus is shown in Fig.10f and is mainly responsible for transporting turbulence from the trough of the wave (region near the free surface) towards the bottom of the flume and the bulk fluid. Melville et. al. [4] also observed and documented the characteristics of this large scale vortex. At t = 0.653 the vortex size grows quite large spanning from x = 2.4 to 3.7 with vorticity $-8s^{-1}$. The vortex is convected downstream at a very low speed, much slower than the mean stream-wise velocity at that location. At t = 0.784 seconds the wave breaking vortex is located at x = 3.1 and has convected only slightly downstream by the mean flow as compared to its initial formation location at x = 2.9. The bump vortex cannot be observed in the CFD vorticity plot, this is due to the differences in the impulsive start conditions. The wave

breaking vortex is clearly demonstrated in the CFD vorticity plot as part of plunging and bubble entrainment events.

At t = -1.307, a region of low *TKE* (0.07 m^2/s) can be observed at the bump vortex location. The remaining region has negligible turbulence. In between $-1.307 \leq t \leq 0$, fairly large values of *TKE* can be seen behind the bump that extends upward under the crest. At t = 0 two distinct regions of high turbulence can be observed. The first region is in between the trough and the crest near the free surface and the second region is well below the free surface in the separated flow. With increasing time in between t = 0 and t = 0.327 the *TKE* level increases near the free surface due to the broken wave and the generation of the wave breaking vortex. The *TKE* dissipates in the separation region as the bump vortex convects downstream and the separated flow region is replaced by high mean stream-wise velocity. Fig.10f shows that after the first plunge the *TKE* level increases by 90% compared to the pre-breaking conditions and after the second plunge it increases an additional 40%. At t = 1.242 the *TKE* near the free surface ($1.2 < z < 1.6$ and $2.4 < x < 3.6$) has reduced and, the region of highest turbulence has swept downstream to $x > 4$. In between t = 1.242 and 1.438, chaotic multiple small scale splash-ups are observed from the PIV images. These small scale splash-ups increase the turbulence level below the breaker only momentarily as can be seen from the *TKE* contours at t = 1.307 seconds. Eventually at a later time step (t = 1.438) the video images show that the aerated region engulfs most of the flow field. The turbulence has also dissipated in the region which was initially most energetic right after breaking. The *TKE* time series (fig.10f) shows that the turbulent levels have dropped by almost 80% compared to the maximum value. Reynolds shear stress contours, $-\overline{u'w'}$ (not shown here) correlated well with mean voticity. It was found that below the breaker in between ($2.5 < x < 3.2$; $0.8 < z < 1.25$) the Reynolds shear stress decay at t^{-1} after the breaking as also observed by [4].

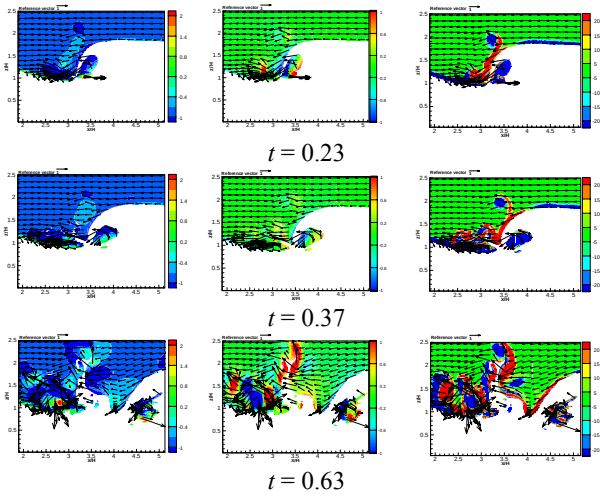

Fig. 14 *U* contours, *W* contours and span-wise vorticity contours for air flows

The axial and vertical velocity contours and span-wise vorticity contours with vectors for air flows are shown in Fig.14. Mean stream-wise velocity is subtracted for clarification as Fig.11 and 12. At t = 0.0 air flows are at rest, while water flows are moving impulsively with 0.87 m/s in the CFD simulations. The impingement of the jet onto the free surface induces strong air flows at t = 0.23, which result in a pair of positive vortices immediately before jet. After falling jet impacts onto trough surface and the splash-up moves upwards at t = 0.37 and t = 0.63, a series of vortices are generated and air flows get stronger because of splash-ups and vertical jet.

8 Conclusions

The present research was able to provide a detailed quantitative description of the overall plunging wave breaking processes through complementary CFD and EFD at their current levels of resolution. Impulsive plunging breaker generated downstream of the bump using accelerated flow was successful in recreating a well controlled breaking wave with typical plunging breaking characteristics for both EFD and CFD. The geometry is different from previous studies and of particular relevance to ship hydrodynamics, since the breaking involves body-wave interactions.

CFD studies revealed that the major events at the early wave breaking stage, such as maximum wave height, first plunge and splash-ups are similar to the observations reported in the literature. Subsequent events are examined and some distinct wave breaking events, such as vertical jet formation, two (even more) repeated processes with reduced amplitudes, chaotic motions and broken wave swept downstream, are identified in the later wave breaking stages. The number of repeated processes likely depends on the acceleration flow conditions. CFD results suggest that the first oblique splash-up appears to rebound from the overturning jet, whereas the first vertical jet originates from the disturbed trough. These major events are mainly identified by CFD and qualitatively confirmed by EFD. More evidence of the wave breaking process hopefully will be obtained from EFD pressure impulse measurements. Pressure impulse measurements likely will correlate with the various events in the wave breaking process. Further investigations using the EFD initial and boundary conditions should be made in order to quantitatively validate the CFD results. Quantitative verification of the 2D-CFD results needs to be further investigated. Due to the two dimensional nature of the present computations with the lack of a mixture model, the two-phase (aerated) region cannot be properly captured and the initially entrapped air bubble behaves differently without the 3D instabilities. A fully 3D large eddy simulation (LES) including surface tension is necessary for a better understanding of the physics of the plunging wave breaking phenomenon. A mixture model is also needed in order to capture the "white water" area generated due to the strong water and air interaction.

An overall description of the organized structures and turbulence associated with plunging breaking wave has also been analyzed in detail using EFD. The close up camera arrangement for test case S1, helped to identify details of the impinging jet and the entrapped air. The jet velocity was calculated to be 0.17 times the mean upstream velocity at t = 0. Vector plots from L1 revealed that the bump vortex is convected downstream below the crest and is an impor-

tant part of the overall flow field. It is also found that the wave breaking vortex generated after the first plunge is convected downstream by the mean flow and is mainly responsible for transporting turbulence from the trough of the wave (region near the free surface) towards the bottom of the flume and the bulk fluid. After $t = 0$, similar flow trends in mean velocity and vorticity is also observed in CFD with more detailed resolutions of plunging, splashing, vertical jet and bubble entrainment. The turbulence is also transported horizontally in the downstream direction by the mean flow. *TKE* contours showed that the first and second plunging events increase the turbulence levels in the trough region by 90% and 130% respectively. Intermittent multiple small scale splash-up events occur after the second plunging that create span-wise vorticity in the trough region. Future EFD work will focus on detailed pressure impulse measurements below the trough region on the flume floor and on the bump surface to obtain a better understanding of how impact pressure affects the body-wave interactions. Further experiments can also be conducted using 3D or Stereo PIV setup to measure the three dimensional and volume flow field in and around the breaker and the instabilities associated with it. So far, literatures on three dimensional studies of plunging breakers are very rare and mostly limited to CFD simulations. Successful 3D-PIV measurements and analysis will be a significant improvement in the overall understanding of the breaking wave.

Acknowledgements

This work is sponsored by the US Office of Naval Research through research grants N00014-01-1-0073 and N00014-06-1-0420 under the administration of Dr. Patrick Purtell. Dr. Suak-Ho Van contributed to the early stages of the EFD. The simulations were performed using DoD HPC resources.

References

[1] Peregrine, D. H. (1983) “Breaking Waves on Beaches”, *Ann. Rev. of Fluid Mech*., Vol. 15, pp. 149-178

[2] Bonmarin, P. (1989) “Geometric properties of deep-water breaking waves”, *J. Fluid Mech.,* Vol. 209, pp.405-433

[3] Tallent, J. R., Yamashita, T., and Tsuchiya, Y. (1990) “Transformation Characteristics of Breaking Waves”, *Wave Water Kinematics*, pp.509-523

[4] Melville, W. K., Veron, F., and White, C. J. (2002) “The Velocity Field under Breaking Waves: Coherent Structures and Turbulence”, *J. Fluid Mech*., Vol. 454, 203-233

[5] Chang, K.-A. & Liu, P. L.-F. (1999) "Experimental investigation of turbulence generated by breaking waves in water of intermediate depth." *Physics of Fluids*, Vol. 11, pp. 3390-3400

[6] Toomas LIIV. (2001) “Investigation of Turbulence in a Plunging Breaking Wave”, *Proc. Estonian Acad. Sci. Eng.,* Vol. 7, pp. 58-78

[7] Watanabe, Y., Saeki, H., and Hosking R. J. (2005) “Three-dimensional Vortx Structures under Breaking Waves”, *J. Fluid Mech*., Vol. 545, 291-328

[8] Yang, J., and Stern, F. (2007a) “Large-Eddy Simulation of Breaking Waves Using Embedded-Boundary/Level-Set Method,” *Proc. 45th AIAA Aerospace Sciences Meeting and Exhibit*, paper 2007-1455, Reno, Nevada

[9] Yang, J., and Stern, F. (2007b) “A Sharp Interface Method for Two-Phase Flows Interacting with Moving Bodies,” *Proc. 18th AIAA Computational Fluid Dynamics Conference*, paper 2007-4578, Miami, Florida

[10] Miyata, M., Matusukawa, C., and Kajitani, H. (1985) “Shallow Water Flow with Seperation and Breaking Wave”, *Autumn Meeting of The Society of Naval Architects of Japan*, November 1985.

[11] Iafrati, A., Mascio, D., and Campana, E. F. (2001) “A Level Set Technique Applied to Unsteady Free Surface Flows, *Int. J. Numer. Methods Fluids*, Vol. 35, pp. 281–297

[12] Huang, J., Pablo, M. C., and Stern, F. (2007) “Couple ghost fluid/two-phase level set method for curvilinear body-fitted grids”, *International Journal for Numerical Methods in Fluids*, March 2007 (in press).

[13] Pope, S. B., “Turbulent Flows” (2000)

[14] AIAA Standard. (1999) “Assessment of experimental uncertainty with application to wind tunnel testing”, *AIAA S-017A*, Washington, D.C.

[15] Yang, J. and Balaras, E. (2006) “An Embedded-Boundary Formulation for Large-eddy Simulation of Turbulent Flows Interacting with Moving Boundaries,” *J. Comp. Phys.*, Vol. 215, pp. 12-40

[16] Enright, D., Fedkiw, R., Ferziger, J., and Mitchell, I. (2002) “A Hybrid Particle Level Set Method for Improved Interface Capturing,” *J. Comput. Phys.*, Vol. 183, pp. 83-116

[17] Sussman, M. and Puckett, E. G. (2000) “A coupled level set and volume-of-fluid method for computing 3D axisymmetric incompressible two-phase flows,” *J. Comput. Phys.* 162, 301

[18] Gueyffier D., Li J. , Nadim A., Scardovelli S., Zaleski S. (1999) “Volume of Fluid interface tracking with smoothed surface stress methods for three-dimensional flows,” *J. Comput Phys*., Vol. 152, pp. 423-456

[19] He, S. & Jackson, J. D. (2000) “A Study of Turbulence under Conditions of Transient Flow in a Pipe”, *J. Fluid Mech*., Vol. 408, pp. 1-38

Table 1 Plunging Wave Breaking Process

	Peregrine (1983)	Bonmarin (1989)	Tallent et. al. (1990)	EFD		CFD
Test setup	Paper is a review article	1. Large air-sea interaction facility (40m long, 3.2m wide and 1m deep) 2. Deep water flow conditions 3. Waves were created by completely immersed electro-hydraulic device 4. Images obtained with powerful flashing lamps and movie camera	1. 36.8 m long wave flume 2. Wave is induced by shoaling on a sloping beach (1/20-1/50) 3. Hydraulically driven piston type wave maker 4. High speed video camera (200fps)	1. Open channel flume (27m long, 0.91m wide, 0.43m deep) 2. INSEAN bump (0.1143m high) 3. 2D-PIV and pitot probes for upstream flow 4. Pitot probe for downstream flow 5. Wave gauges for air-water interface elevation 6. 2D-PIV in the breaking wave region		1. Computational domain is 5H × 96H for 2D, 5H × 96H ×0.4l for 3D. (H=0.1143m, bump height; l=0.2758m, bump length) 2.Grid size 768 × 256 for 2D and 768 × 256× 32 for 3D 3. Re= 99441 and Fr=0.82 4. Initial time step is 5 × 10-5 and is reduced to 1 × 10-5 later
Steep Wave Formation	1. An element of the water surface becomes vertical.	1.Crest steepens and becomes vertical. a. Wave height is 9.5 cm b.Wave steepness is ak=0.386 c. Breaking coefficient = 0.02		**Max height**	1. At time t=0 (t_b=12.37sec) the wave crest is the steepest and reaches the maximum height. a. Wave height is 11 cm (0.96H). b. Wave steepness is ak=1.36.	1. At time **t=0** (t_b=0.49 sec), the wave crest is the steepest and reaches the maximum height. a. Wave height is 7.43 cm (0.65H). b. Wave steepness is ak =1.23.
Crest Over-turning	2. A portion of the surface overturns. Main features: Water-particle velocity exceeds wave velocity; water accelera-tions exceed gravity acceleration in a thin region of the front of the wave. New's ellipse fit is used for the air bubble, the aspect ratio is √3. Jet direc-tion (angle) varies and can be vertical. Duration of overturning is unknown.	2. A jet of water is projected forward into a characteristic overturning motion. The surface profile beneath the over-turning crest is approximated by New's ellipse model with an aspect ratio of √3. The accurate fit is used in Fig 18, the aspect ratio changes from 2.33 to 1.36, 1.49 and 1.61.	1. The wave crest overturns and initial penetration of the jet into the trough occurs. A primary eddy beneath the jet is formed. 2. The eddy shape is nearly elliptical and the steep angle is approximately 45-50 degrees.	**First plunge**	2. The overturned crest touches the main water body at **t=0.065**. This can be referred to as the **first plunge**. a. Jet velocity, w = - 0.07m/s. b. Width of jet = 4.9% of the maximum wave height. The initial volume of the tip of the jet that begins to enter the trough region is quite small. A gentle splash up region can be ob-served at x = 2.4.	2. The jet overturns, the jet angle (with horizontal free surface) reaches approximately 50 degrees at t=0.16. Air enclosed has an elliptical shape, with an aspect ratio of 2.15.
Splash-up	3. The jet hits the water at the plunge point; water splashes up with a height greater than the original wave. From the plunge point onwards, the breaking process rapidly degenerates to a chaotic motion of air and water. Three possible modes of the origin of splash-up: the jet "rebounds"; "pushes up" the undisturbed trough fluid; and combina-tion of the above two modes. The splash is usually projected forward to hit the undisturbed water at a second plunge point.	3. As the falling jet hits the undisturbed water surface in front of the crest, some water splashes up. Two large vortices are formed with opposite rotation directions. The splash-up is projected at different angle: forward, back ward or straight up. The splash-up initially comes from trough and later more from plunging crest.	3. As wave propagates the splash up initiates at the location of the jet impact at 0.27 seconds. The steep angle continues to increase. 4. The splash-up emerges as a fine fan shaped "spray (high air content)", fol-lowed by the eruption of a nearly vertical splash up "core (low air content)". "Spray" originates from both overturning jet and trough surface; "core" from trough alone. "Spray" and "core" initiate at 0.27 and 0.325 seconds respectively. 5. A pair of counter rotating eddies are formed by the overturning fluids at 0.42: primary eddy (clockwise) and secondary eddy (counter clockwise). At t=0.44 sec, the wave elevation begins to decay. 6. The splash-up core angle and elevation growth decrease rapidly; finally a second-ary eddy is observed.			3. At **t=0.23**, 1st plunge occurs when the jet hits the trough surface. Air bubble is entrapped and 1st splash-up initiates.
				Oblique splash	3. At **t=0.196** the **splash-up** that began at t=0.131 starts to intensify and occurs at an oblique angle with respect to the vertical direction. The air bubble can also be ob-served in the PIV image if looked closely, but not as clearly as the video image.	4. At **t=0.37**, splash-up intensifies; an oblique jet is projected forward with a spray region of small droplets. The entrapped air bubble starts to move to downstream with its shape deformed.
				Vertical jet	4. At **t=0.327** the splash-up intensifies reach-ing a maximum height of ζ = 2.22. A spray zone forms in between x = 2.1 and x = 3.25. A **vertical jet** at x = 3.05 is ejected from the trough.	5. After the oblique jet impact onto the trough surface, a vertical jet starts to be formed and reaches its maximum height of ζ = 2.15 at **t=0.63**, which is higher than the original wave.
Air entrainment	4. Air beneath forms a tube. No rapid collapse occurs because air pressure and centrifugal acceleration balance inward pressure. The air bubble can have a short life due to the non-circular initial state and three-dimensional instability.	4. The air bubble entrapped by the overturning jet, or entrapped between the falling jet and splash-up		5. The entrapped air bubble can be seen at **t=0.327** seconds with its center at x = 3.6.		6. Although the initially entrapped air bubble expe-riences severe shape deformation, it does not collapse and continues moving downstream.
Subsequent Events	5. Several splash-up cycles can occur. The vortex-like motions from each cycle all have the same direction of rotation with rapid decrease in wave height and energy loss.	5. After 1st splash-up the flow can either directly degenerate into a chaotic motion or displays a relative order in the form of successive splash- up cycles and vortices which are less and less active.	7. Splash-up begins to collapse once it reaches maximum height, and a new fluid circulation initiates. Maximum splash-up is at 0.56 seconds. 8. A subsequent pair of counter rotating eddies are formed which eventually initiates a second fluid splash-up that is slightly smaller, and the process contin-ues.	**Second plunge**	6. At **t=0.653** the second plunge occurs	7. The vertical jet deceases in height and the 2nd jet is formed, when time reaches **t=0.79**, the 2nd plunge occurs. The initially entrapped air bubble has been swept downstream.
				Second oblique splash	7. At **t=0.719** the PIV image shows the **second oblique splash-up**. Ejections of small volumes of fluids can be seen at x = 2.6 and 2.75 in the PIV image.	8. The 2nd oblique splash-ups can be found at **t=0.87**.
				Second vertical jet	8. At **t=0.784** a small vertical jet can be ob-served from the video image at x = 3.35.	9. 2nd vertical jet is formed at **t=0.95.**
				Third plunge	9. At **t=1.242** seconds the second splash-up plunges again. This will be referred to as the **third plunge**.	10. At **t=1.07**, the 3rd plunge occurs.
				Chaotic repeat	10. At **t=1.307** repeatable multiple splash-ups occur	11. At **t=1.31**, chaotic splash-ups occur
				Wave has swept downstream,	11. The PIV image at **t=1.438** shows that the broken wave has swept downstream.	12. After **t=1.31**, breaking flow is swept downstream with multiple small scale splash-ups and jets.

Table 2 Velocity, vorticity and turbulence flow fields inside plunging breakers

	Melville (2002)	Chang & Liu (1999)	Toomas (2001)	Watanabe et al.(2005)	EFD	CFD
Test Setup	1. Glass wave channel, 30 m long, 0.5 m wide, and water depth of 0.6 m (deep water waves) 2. Inclined beach 3. DPIV with laser light sheet 4. CCD camera	1. Wave tank of 30 m long, 0.6 m wide and water depth of 0.2 m (intimidate depth) 2. A beach of 1/10 slope at the end of the tank 3. 2D PIV with light sheet fired 4. Repeated measurements for 25 times	1. A Wave flume of 0.6 m wide, 0.6 m deep, and 2 2m long was used. 2. A computer controlled wave generator was used 3. Velocity distribution was measured using a two-component LDA in wave breaking region.	1.3D LES with a single-phase free surface model is used 2. Computational grid is564 × 26× 41 3. Conidial wave modulus: 0.99470; wave height:0.58; water depth: 0.57; bottom slope: 1/20; Surface similarity parameter: 0.4510; wave period: 2.75 sec. 4. Periodic BC in y direction; non-slip at bottom and constant pressure at top; numerical wave maker is located at the inlet.	1. Open channel flume with bottom bumps 2. Measurements obtained: 2D PIV in the breaking region, Air-water interface elevation, Upstream and downstream velocities and flow rates	1. Computational domain is 5H × 96H for 2D, 5H × 96H ×0.4*l* for 3D. (H=0.1143m, bump height; *l*=0.2758m, bump length) 2.Grid size 768 × 256 for 2D and 768 × 256× 32 for 3D 3. Re= 99441 and Fr=0.82 4. Initial time step is 5 × 10-5 and is reduced to 1 × 10-5 later
Velocity and Vorticity	1. At the first few times, large orbital velocities are shown as the waves propagate 2.Coherent vortex of positive vorticity (clockwise) propagates downstream and deepens 3. The magnitude of mean vorticity decreases from 0.5 to 0.04, while it deepens from z=0.02 to 0.05.	1 .The breaking jet has a velocity of 1.5*C*, whereas the velocity under the aerated region is less than *C*/2. *C* is the wave phase speed. 2. The order of magnitude of mean vorticity was small outside the aerated region, compared to the instantaneous vorticity. 3. The maximum mean vorticity was $-C/h$, where h is the local water depth at the breaking point.	1. Horizontal velocities are 0.35C under crest and -0.3C under the trough (C, local phase velocity) at wave breaking instant. 2. The maximum vertical velocity is approximately 0.08C under the wave crest. 3. One acceleration and deceleration regions exist for the horizontal velocity component. 4. The vertical velocity component changes its sign at the end of the deceleration of the horizontal velocity, which indicates a change of direction of the large scale eddies.	1. The vorticity becomes unstable at the region of the plunge point, and a 3D velocity field is triggered simultaneously. Spanwise vorticity undulations are caused. 2. The undulations are amplified, a vortex loop with counter-rotating vorticity is formed 3. A typical rib structure is formed with the adjacent primary vortices enveloped by the vortex loop. 4. This rib structure intensifies in the strains associated with multiple primary vortices generated throughout splash-up cycle.	1. Zoomed in PIV imaging helped to measure jet velocity and thickness 2. Bluff body vortex shed from bump does not significantly affect the breaking process. 3. Image pre processing helped to measure velocity and vorticity in the two-phase region. Primary vortex, has maximum value of 12.6s^{-1}. 4. Sub-sequent small scale vortices are formed due to multiple splash-ups.	**Velocity (stream-wise)** 1. At max height, two reverse flow zones initiate: one at the tip of the crest and the other behind the bump. 2. The reverse flow at the crest intensifies as the jet overturns; the reverse flow zone behind the bump develops into a thin layer at the bottom. **Vorticity** 1. Before jet overturns, positive vorticity can be found near the tip of the jets, which is caused by strong air flows 2. After the jet overturns, the primary anti-clockwise vortex develops 3. A positive vortex is formed at the saddle region between the splash-up and the original crest
Turbulence	1. At the beginning, kinetic energy of the mean flow associated with the vortex propagating downstream is dominant and advected slowly downstream at later times. 2. At the later times, the Reynolds stress is predominantly negative, corresponding to the downward transport of positive horizontal momentum. 3. TKE, vorticity, and Reynolds stress decay at the rate proportional to inverse of time.	1. Turbulent velocity is an order of magnitude smaller than the phase velocity under the trough level. 2. Diffusive term in turbulent kinetic energy transport equation is an order of magnitude smaller than the rest of terms. 3. The turbulence dissipation is smaller than the turbulence transport term throughout the measurements. 4. The time scale of turbulent decay rate reaches unity after four breaking waves.	1. Turbulent intensities are highest during overturning. 2. Wave breaking generates an extra source of turbulence near the free surface, turbulence intensity increases. 3. Large scale eddies carry energy away from surface. 4. Turbulence decays rapidly after passage of crest. 5. Acceleration damps turbulent fluctuations so in the areas of highest acceleration, there are lowest turbulent intensities. 6. Turbulent kinetic energy is highest right before and under the wave crest and decreases rapidly in the wave trough. 7. Most of the energy is produced at the instant when the wave breaks. The energy level decreases toward the bottom.		1. *TKE* levels are low prior to breaking. After breaking *TKE* is high right below the free surface and spreads inside the aerated region. 2. The first splash-up creates high levels of turbulence. The turbulence level increases after the second splash up due to the combined effects of both splash-ups. 3. Regions of high *TKE* levels range from x = 2.2 to 3.5 4. At 0.719 sec. after breaking, regions of high *TKE* levels begin to advect downstream.	1. Further investigation of TKE and Reynolds stress by 3D LES will be in the future work

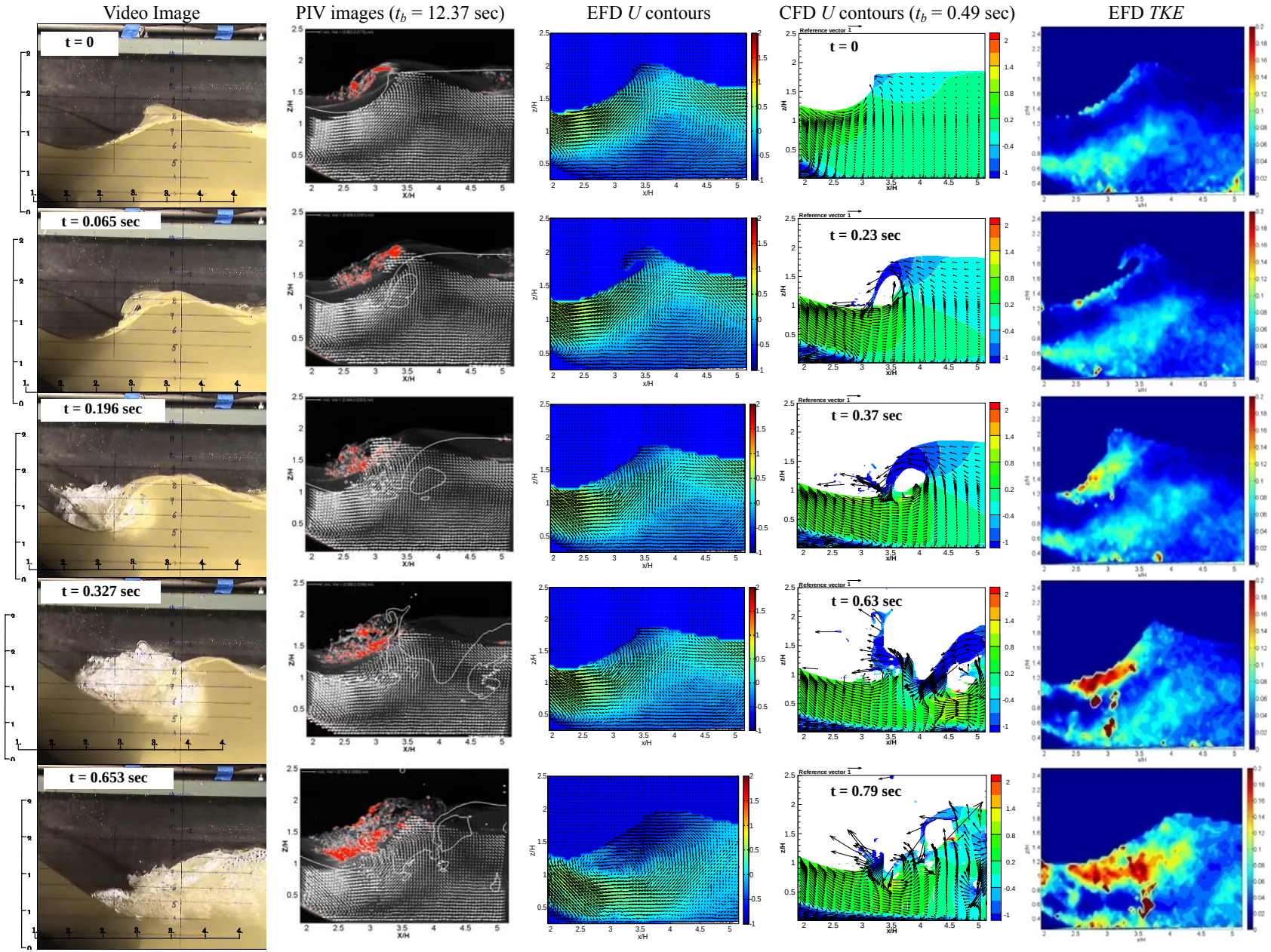

Fig. 11 Video image, PIV image with overlaid CFD wave profile, EFD U contours, CFD U contours and TKE at different time steps

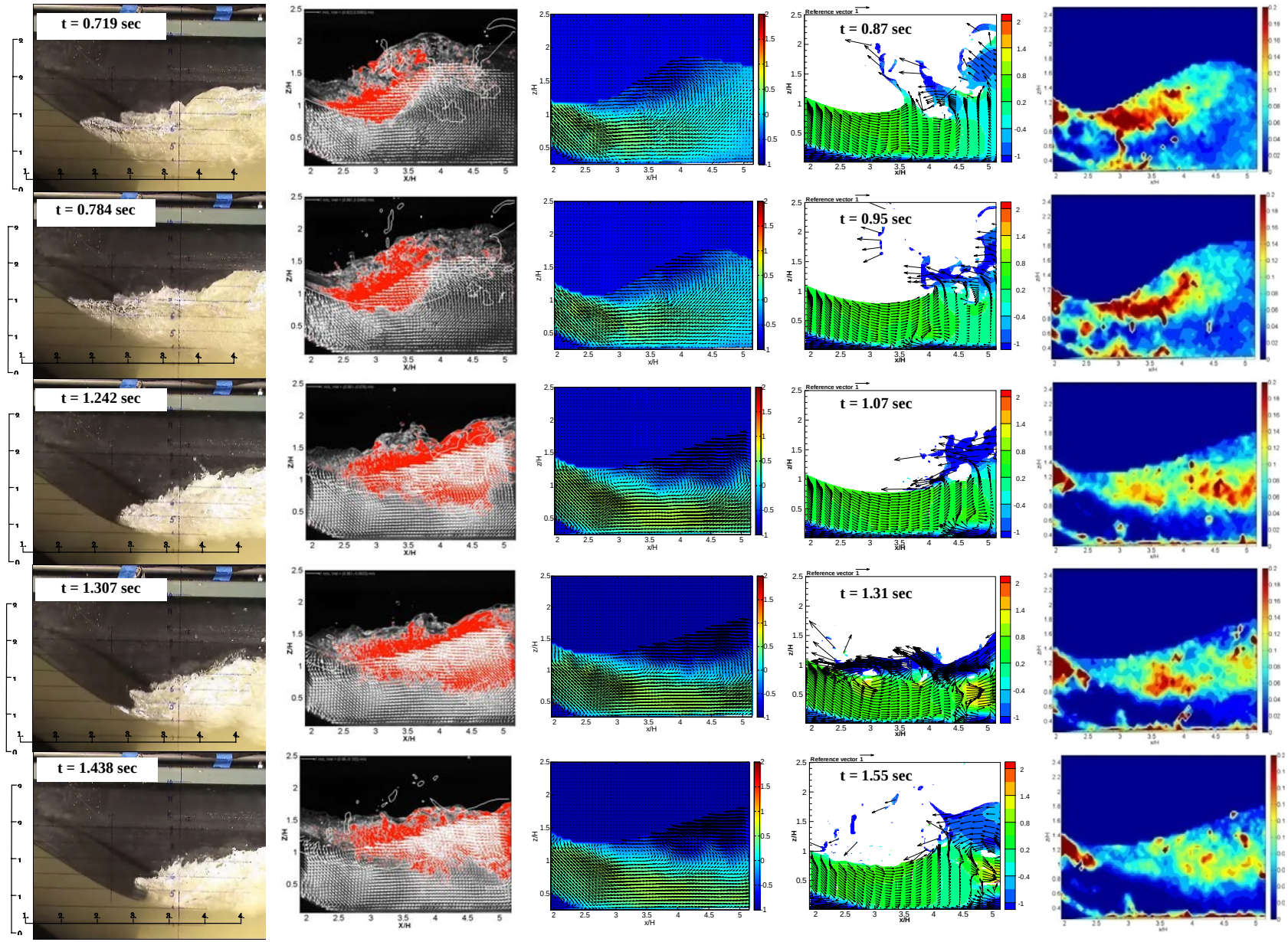

Fig. 11 (continued)

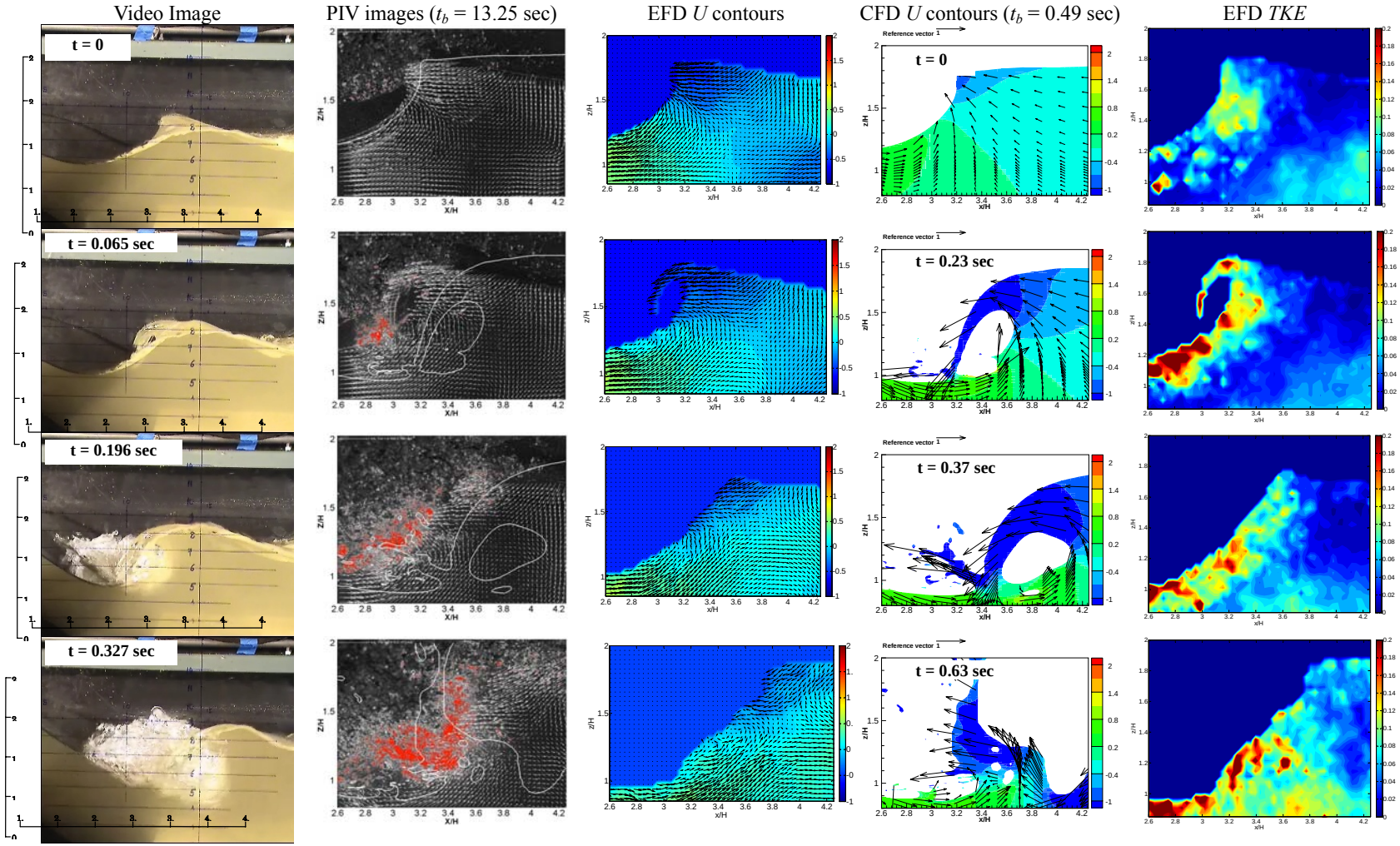

Fig. 12 Video image, PIV image with overlaid CFD wave profile, EFD *U* contours, CFD *U* contours and *TKE* at different time steps for test case S1